Lawrence Berkeley Laboratory
UNIVERSITY OF CALIFORNIA

Materials & Chemical Sciences Division

Crack Growth Behavior of Encapsulation Processed SiC-PMMA Particulate Composites

C.H. Sheu
(M.S. Thesis)

May 1990

LOAN COPY
Circulates
for 2 weeks
LBL-29611
Copy 2
Bldg. 50 Library.

Prepared for the U.S. Department of Energy under Contract Number DE-AC03-76SF00098.

DISCLAIMER

This document was prepared as an account of work sponsored by the United States Government. While this document is believed to contain correct information, neither the United States Government nor any agency thereof, nor the Regents of the University of California, nor any of their employees, makes any warranty, express or implied, or assumes any legal responsibility for the accuracy, completeness, or usefulness of any information, apparatus, product, or process disclosed, or represents that its use would not infringe privately owned rights. Reference herein to any specific commercial product, process, or service by its trade name, trademark, manufacturer, or otherwise, does not necessarily constitute or imply its endorsement, recommendation, or favoring by the United States Government or any agency thereof, or the Regents of the University of California. The views and opinions of authors expressed herein do not necessarily state or reflect those of the United States Government or any agency thereof or the Regents of the University of California.

Crack Growth Behavior of Encapsulation Processed SiC-PMMA Particulate Composites

Chi Hsien Sheu

Center for Advanced Materials
Materials and Chemical Sciences Division
Lawrence Berkeley Laboratory

and

Dept. of Materials Science and Mineral Engineering
University of California
Berkeley, CA 94720

May, 1990

This work was supported by the Division of Materials Sciences, Office of Basic Energy Sciences, United States Department of Energy under Contract No. DE-AC03-76SF00098.

Crack Growth Behavior of Encapsulation Processed SiC-PMMA Particulate Composites

Chi Hsien Sheu

Center for Advanced Materials
Materials and Chemical Sciences Division
Lawrence Berkeley Laboratory

and

Dept. of Materials Science and Mineral Engineering
University of California
Berkeley, CA 94720

Abstract

The effect of processing on the fatigue crack propagation and fracture toughness of ceramic-polymer composites was investigated. A new process for composite production was developed with homogeneous particle distribution and low residual stress levels in mind. PMMA was uniformly distributed by encapsulating the SiC substrate by means of precipitation polymerization. The encapsulation processed powders were then compacted at temperatures above T_g to form the composite.

The encapsulation process was optimized by varying the initial concentrations of the reactants until homogeneous nucleation was suppressed. The coatings were found to be continuous at the SiC-PMMA interface, with particle agglomeration occurring between coated particles. Polymer loadings equivalent to 30 vol% SiC were achieved.

Composites of several particle size ranges were tested under cyclic fatigue and static loading conditions. Fatigue growth rates and fracture toughness data display a trend of increasing crack growth resistance with increasing particle size, with encapsulation processed composites outperforming conventionally cast composites in both cyclic fatigue and fracture resistance. The largest K_{Ic} value was found to be 2.95 MPa(m)$^{1/2}$, a factor of 3 increase over un-reinforced PMMA. The roles of crack deflection, shielding, bridging, and pinning in enhancing toughness were discussed in light of crack profile and fracture surface details.

Table of Contents

Acknowledgements iv

1. Introduction 1

    1.1. Reinforced Polymer Composites 1

    1.2. Silicon Carbide as Reinforcement 2

    1.3. Polymethyl Methacrylate 2

    1.4. Conventional Polymer-Ceramic Processing 4

    1.5. Encapsulation Processing 5

2. Encapsulation Processing 8

    2.1. Emulsion Polymerization 8

    2.2. Precipitation Polymerization 9

    2.3. Encapsulation Processing Optimization 10

    2.4. Powder Characterization 12

        2.4.1. Scanning Electron Microscopy 12

        2.4.2. Transmission Electron Microscopy 12

    2.5. Results 13

    2.6. Discussion 17

3. Crack Growth Behavior of Particulate Composites 21

    3.1. Crack Pinning 21

    3.2. Crack Deflection 26

    3.3. Crack Tip Shielding 26

        3.3.1. Frontal Process Zone 27

        3.3.2. Process Zone Wake 27

    3.4. Crack Bridging Mechanisms 29

        3.4.1. Co-planar Uncracked Ligaments 29

        3.4.2. Overlapping Crack Ligaments 30

    3.5. Experimental 32

3.5.1. Encapsulation Processed Composite Forming 32

3.5.2. Conventional Composite Casting 32

3.5.3. Subcritical Crack-Growth Testing 34

3.5.4. Fracture Toughness Measurements 37

3.6. Results 37

3.6.1. Crack-Growth Rates 39

3.6.2. Fracture Toughness 39

3.6.3. Microstructural Examination 45

3.7. Discussion 59

4. Summary 65

References 66

Acknowledgements

The author would like to thank all those individuals who helped made this work possible. My special thanks go to Professor Lutgard DeJonghe for his guidance and tutelage; Reiner Dauskardt for his time and unsurpassed knowledge in the mechanical testing of my specimens; Yves Boiteux for his TEM work; and all the members present and past of my research group who helped make my stay so enjoyable.

1. Introduction

1.1. Reinforced Polymer Composites

Reinforced composite materials are one of the major material advances of this century. The ability to combine the physical and mechanical attributes of vastly different materials has led to a boon in many engineering fields, including the aeronautical/aerospace, automotive, electronics, and the marine industries.[1-5] These materials revolutionized each field with their enhanced strength and reduced weight. Although there were early problems with the implementation of such anisotropic materials, they were quickly overcome, thereby opening the door for the tremendous advancements that have been made to date.[1,6] However, the acceptance of polymer composite materials in engineering is still more difficult than for metallics due to the added knowledge of the mechanical behavior required for their application. Therefore, a good understanding of the fundamental properties of these materials is extremely important to ease the transition from metals to composites.[7,8] Many studies have been made on the properties of particulate reinforced polymer composites for this reason.[9-19]

In addition to structural applications, reinforced polymer composites have been investigated for their electric, dielectric, and pyroelectric properties.[20,21] Because of the wide range of matrix and filler components available, a reinforced polymer composite can be engineered to fill almost any specialty electronics application. Often, the combination of properties afforded by these materials cannot be matched by conventional metallics.

More recently, polymer-ceramic processing methods have been investigated for use in producing homogeneous green body compacts in the field of ceramic materials.[22,23] Heterogeneities in ceramic green bodies greatly impede uniform densification of the ceramic.[24] In addition to minimizing agglomeration and other inhomogeneities, the polymer phase acts as a binding agent which aids in the fabrication of complex shapes. Once the product has been compounded, it can then be easily pressed or drawn into

complex shapes. This process results in compacts with much improved green strengths, making handling less difficult.

1.2. Silicon Carbide as Reinforcement

Ceramics are an excellent choice as a reinforcing phase in polymers for a wide variety of specialized applications. In addition to modulus improvements, other specific properties may be imparted, including abrasion resistance,[3] fire retardancy,[2,6] dielectric constant modification,[4] etc. Of special interest are applications where friction and wear are present, but lubrication may be difficult, if not impossible, i.e., dry bearings, gears, etc. Several studies of ceramic-polymer composites have been undertaken in these areas.[25,26] Silicon carbide demonstrates superior abrasion resistance, thermal conductivity, and hardness, making it very attractive for such high wear environments.[2,6] Typical properties of silicon carbide are given in Table I.

1.3. Polymethyl Methacrylate

Polymethyl methacrylate (PMMA) is a member of the acrylic family and is widely known by its tradenames: "Plexiglas" and "Lucite." The structure of PMMA is given in Figure 1.1. Polymethyl methacrylate is classified as a thermoplastic polymer, meaning that it can be plastically deformed or shaped above its glass transition temperature (T_g) to form the final product shape. These polymers can be deformed repeatedly without diminishing their properties. By contrast, thermoset polymers are dry pressed into their final shape and then fired. Once cross-linking occurs, the shape can no longer be altered. Typical properties of PMMA are also given in Table I. PMMA is used in an extremely wide variety of applications and industries.

Typical values for:	Silicon carbide	Polymethyl methacrylate
Density ρ (g/cm^3)	3.21	1.2
Young's Modulus E (GPa)	450	3
Yield Strength σ_y (MPa)	10,000	60-110
Tensile Strength (MPa)	–	110
K_{Ic} (MPa(m)$^{1/2}$)	3	0.8-1.4
Expansion Coeff. α (/°K)	3×10^{-6}	61×10^{-6}
T_g (°C)	–	120

Table I Comparison of typical properties of silicon carbide and polymethyl methacrylate.

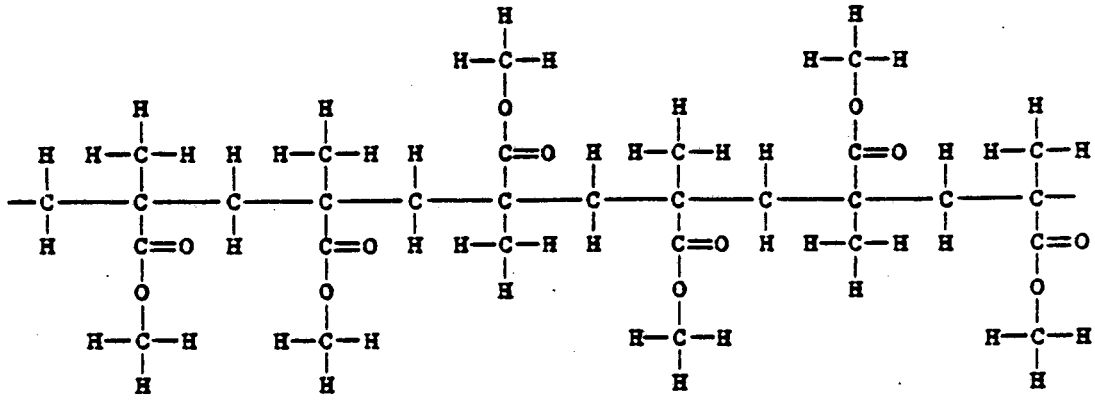

Figure 1.1 Structure of polymethyl methacrylate.

1.4. Conventional Polymer-Ceramic Processing

Traditionally, polymer-ceramic composites have been formed by compounding processes followed by molding processes. Depending upon the polymer system considered, the process may involve either a viscous polymer blend, or *in-situ* polymerization. The ceramic phase is typically compounded using a high shear mixing process. Commercially available equipment such as twin roll mills and twin screw extruders are suitable for this application.

There are several important limitations to this processing route, the first of which is finite wetting of the ceramic phase. If the slurry viscosity is too high, incomplete wetting may lead to substantial agglomeration of the ceramic phase. Agglomeration of a dispersed second phase has been shown to influence strongly the mechanical properties of these composites,[27] and depending upon the nature of the agglomerates, these influences may be positive or negative.[28] For strong agglomerates, mechanical properties are enhanced due to an increase in polymer filling caused by air trapped within agglomerate clusters. The macroscopic effect is an apparent increase in the volume fraction of the reinforcing phase. On the other hand, weak agglomerates tend to break up at low applied stresses and therefore act as crack initiation sites. These cracks degrade the material and diminish the mechanical properties of the composite.

In addition to agglomeration, the compounding process may introduce porosity in the composite by air trapping. These pores play the same role as weak agglomerates in the degradation of the composite. Although controlled micro-porosity may actually increase the fracture resistance of the material,[29] macroscopic uncontrolled porosity should be avoided.

Yet another limitation to high shear mixing is the viscosity of the polymer blend. As either the volume fraction of the reinforcing phase increases or the average particle size decreases, the blend viscosity increases, hindering the uniform dispersion of the reinforcing phase. This is exacerbated at very small particle size ranges, since uniform

dispersions are more critical for homogeneous densification during sintering when the starting powders become finer.[23] During high shear mixing, degradation of polymer blends may also occur, increasing as the second phase dispersions become finer. The processing must therefore be carefully controlled to minimize the amount of degradation while maximizing filler content and dispersion uniformity.

Finally, thermal expansion mismatch between the two phases introduces significant residual stresses, which may cause shrinkage cracking as well as weaken the particle-matrix interface.[30] The effect of these stresses on the mechanical properties of the composite is dependent upon the particular active mechanism.[31,32]

Certain forming processes, such as injection molding, may also contribute to inhomogeneous distributions of second phase particles.[33] Both longitudinal as well has cross-sectional inhomogeneities may occur. As the reinforcing phase moves away from cavity walls during injection, migration into a region of higher fluid velocity occurs. This effect produces a cross-sectional composition gradient which also leads to a longitudinal gradient down the length of the piece.

1.5. Encapsulation Processing

The numerous limitations in traditional processing technologies reveal a need to investigate alternative production methods. A process which improves the distribution of second phase particles should greatly enhance the mechanical properties of these composites and any final products derived from them. In addition, specialized applications which require very homogeneous dispersions, such as ceramic processing, can greatly benefit from improved processing technology.

Encapsulation may provide a new means of producing homogeneous particle distributions in polymers. By distributing the polymer uniformly around each particle, the amount of agglomeration will be reduced and, since no viscosity effects are present, the maximum filler content is not restricted. Figure 1.2 illustrates the idea behind

encapsulation processing. Each discrete unit will ideally be a packet of one second phase particle surrounded by the appropriate amount of polymer. The powder in this configuration can easily be molded using any existing dry press forming technique.[34] The powder is consolidated by heating above T_g to form the composite.

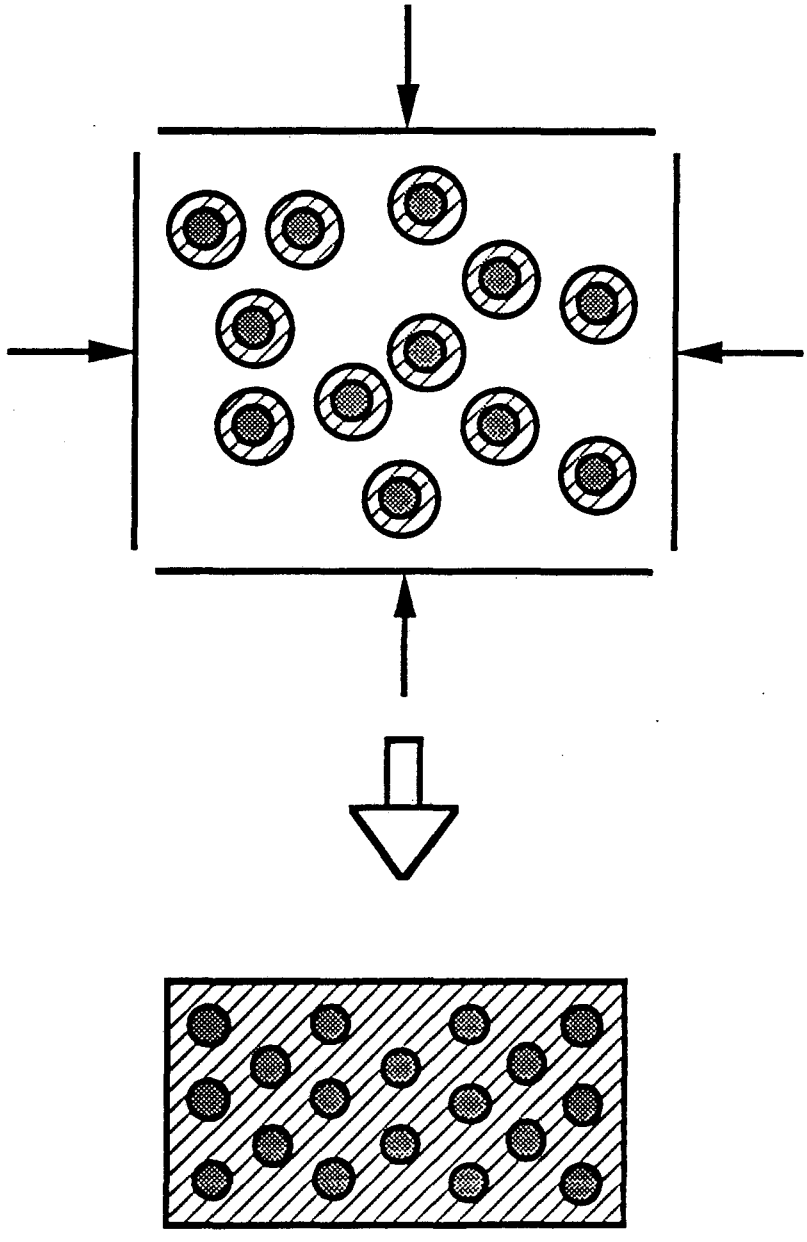

Figure 1.2 Encapsulation processed composite forming.

2. Encapsulation Processing

2.1. Emulsion Polymerization

Although emulsion polymerization is a popular choice for the commercial production of polymers, there are many limitations when used as a means for particle encapsulation. In general, the process occurs in an aqueous medium by means of free-radical polymerization mechanisms. Typical emulsions contain the following ingredients: hydrophobic monomer, water-soluble initiator, and emulsifier, while other minor ingredients, such as chain-transfer agents, may also be present. Some form of agitation is usually required to maintain the suspension.

The specific physical and chemical reaction mechanisms in emulsion polymerization are significantly influenced by the heterogeneous nature of the system, and can thus have a large effect on the final product. It is therefore natural to assume that this heterogeneous nature can be harnessed for nucleation and polymerization on particle surfaces. However, this is not necessarily the case.

In an emulsion system, the most obvious sites for polymer nucleation would be inside the monomer droplets. However, as the particle yield of the process is usually two to four orders of magnitude greater than the initial number of monomer droplets, polymerization within the droplets is not generally considered significant.[35] More often, the monomer droplets act as reservoirs for the polymerization process. Since there is a finite solubility of monomer in the aqueous medium, the formation of monomer-swollen micelles occurs. These micelles are readily accessible to the water-soluble initiator, and are therefore the dominant sites for polymer nucleation. However, monomer droplet initiation can be a dominant polymerization process in limited circumstances.[36]

When the water solubility of the monomer is relatively high, as is the case with PMMA,[37] homogeneous nucleation poses significant barriers to the encapsulation process. In such cases, a polymer surface treatment of the particulate would be necessary.[38] These

polymers act as anchor sites for newly formed emulsion polymer particles. As polymerization proceeds, the particles are eventually encapsulated.

2.2. Precipitation Polymerization

Due to the many limitations of the emulsion polymerization process, the precipitation polymerization method of particle encapsulation was investigated.

Precipitation polymerization has several advantages over other polymerization methods as an encapsulation process. First, no surface active agent is necessary to ensure encapsulation, as would be the case for monomer droplet initiated emulsion systems. Second, no polymer pre-treatment of particles is required, as no polymer anchor sites are needed as with micelle initiated emulsion systems. Finally, the polarity of the polymerization medium need not be considered, since zeta potential and double layer charge effects are not present.

Precipitation polymerization is based on a reaction medium which is capable of dissolving polymer precursors and any polymerization initiators, but which acts as a non-solvent for the polymer product. The product of a polymerization reaction should therefore precipitate out of solution, with any particles suspended in solution becoming preferential nucleation sites for the precipitated polymer. After nucleation, polymerization proceeds on the particle surfaces, eventually encapsulating the particle.

Unlike emulsion polymerization batch processes, in which all starting ingredients are added initially, the reactants in a precipitation polymerization process typically are introduced into the reaction medium simultaneously over time at a rate sufficient to avoid excess monomer concentration. Excessive monomer concentration produces two unwanted results: polymerization occurs homogeneously in solution, and the polymer tends to agglomerate on the surface of the particles to be coated. The rate of reactant addition must therefore be closely controlled.

The best reaction mediums are the non-polar, straight chain aliphatic hydrocarbons, such as hexane and heptane. Mixtures of solvents are also acceptable. The non-polar nature of these solvents makes particulate suspension difficult however, so some form of mechanical agitation is required to maintain these suspensions.

Precipitation polymerization requires that a suitably soluble initiator be employed. Benzoyl peroxide is a oil-based initiator used in the polymerization of methyl methacrylate that has been found to be soluble in toluene, which can be mixed with hexane during reaction.

Polymethyl methacrylate has been successfully precipitated on silica using this method.[39] The precipitation of methyl methacrylate on silicon carbide should proceed in a similar manner, as surface characterization studies on silicon carbide reveal that an amorphous oxide layer exists on the surface of silicon carbide which resembles that of silica.[40,41] This method has successfully produced coatings on substrates particle sizes ranging from 0.1 μm to 100 μm or more.[39]

2.3. Encapsulation Processing Optimization

β–silicon carbide powder (Superior Graphite HSC - nominally 1μm) was prepared by mechanical grinding followed by sieving to remove large agglomerates and any coarse fractions. To break up any remaining agglomeration, a measured quantity was then ultrasonically dispersed in a distillation flask containing 150 ml hexane. The solution was heated to boiling under a distillation column and agitated by means of a magnetic stirring plate in order to maintain suspension. Methyl methacrylate was separately dissolved into 50 ml of hexane. The proper ratio of silicon carbide to methyl methacrylate was determined by trial and error. One wt% benzoyl peroxide (initiator) was dissolved into 3 ml toluene and drawn into a syringe.

The experimental apparatus is shown in Figure 2.1. The prepared solutions were introduced dropwise to the suspension over a period of two hours with agitation, and

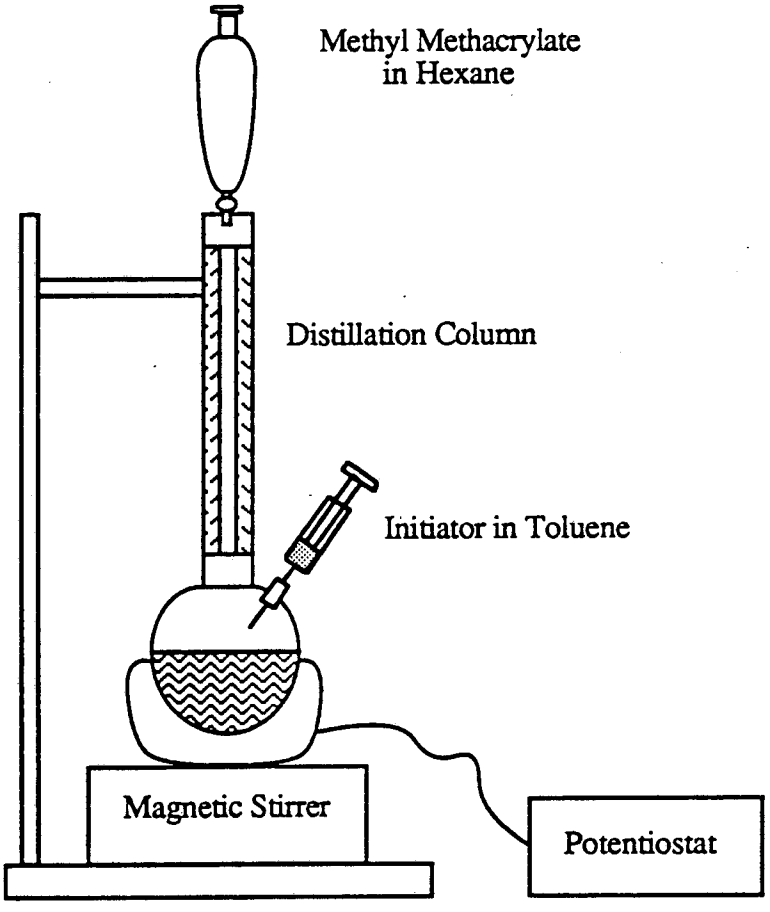

Figure 2.1 Experimental apparatus.

allowed to react for an additional two hours. The reaction product was poured into a large beaker, and the excess solvent decanted. The remaining slurry was allowed to stand overnight to evaporate until a firm consistency was reached. Finally, the slurry was vacuum dried for two hours to remove any remaining solvent, thus forming a powder cake. Alternatively, the suspension can be spray dried to produce the final powder product.

2.4. Powder Characterization

2.4.1. Scanning Electron Microscopy

Scanning electron microscopy is a very useful tool for examining the morphology of powders, coatings, and surfaces. Features such as particle size, particle shape, coating effectiveness, etc., can readily be seen. In addition, features such as fracture surfaces and polished cross-sections can be studied.

As-received powder samples for SEM examination were prepared by first mechanically grinding to remove agglomerates, followed by pressing onto conducting adhesive affixed to specimen stubs. Precipitation encapsulated samples were prepared by first extracting a small amount of reaction product, typically on the order of 1cc. This was done before decanting the solvent. One to two drops were then placed on a specimen stub and allowed to dry. This technique has the advantage of not requiring a re-dispersion of the powder in a solvent, which could possibly damage the polymer coating. Furthermore, no additional grinding is required. Since these samples were non-conductive, the stubs were gold coated to minimize any surface charging effects from the electron beam.

The samples were examined under a 5-20kV electron beam. The choice of accelerating voltage depended upon the sensitivity of the sample to surface charging and beam damage. Magnifications ranged from 50x to over 15kx.

2.4.2. Transmission Electron Microscopy

The 1.5 MeV electron microscope at the National Center for Electron Microscopy at the Lawrence Berkeley Laboratory was used to examine the interior features of the

precipitation coated powders. The microscope allowed direct observation of the silicon carbide-PMMA interfaces. Although, theoretically, any agglomeration of silicon carbide within individual polymer capsules can be seen, particle overlap may obscure some details. However, polymer coating thicknesses can be easily measured, thus providing important information on the effectiveness of the encapsulation process.

The TEM samples were prepared by a technique similar to SEM sample preparation. A drop of the powder-containing solvent was carefully deposited onto a 3 mm copper grid of 300 mesh supplied by Ted Pella, Inc. The solvent was allowed to evaporate, leaving a thin layer of encapsulated silicon carbide on the grid surface.

2.5. Results

The as-received β–silicon carbide powder contained large agglomerates of sizes ranging to several millimeters as seen in Figure 2.2. Mechanical grinding was employed to remove these macroscopic agglomerates, resulting in the powder of Figure 2.3. The β–SiC particles are multi-faceted, roughly equiaxed and exist in an approximately bimodal distribution. The small fraction is on the order of 0.3 μm, while the large fraction is on the order of 1 μm.

Homogeneous precipitation results of PMMA are shown in Figure 2.4. The precipitated latex particles are spherical and roughly uniform in size. The average size of the particles is approximately 0.2 microns. The particles have agglomerated into a interconnected three dimensional network with polymer bridges similar to necks observed in the sintering of ceramic materials.

Figure 2.5 shows the powder after the initial precipitation encapsulation attempt. It is clear that homogeneous nucleation was not suppressed, indicating that the process variables were not optimized for encapsulation. Figure 2.6 shows the precipitation results after adjusting the initial concentration of reactants. Although the encapsulated powder is agglomerated, each individual particle appears to be fully coated, with agglomeration

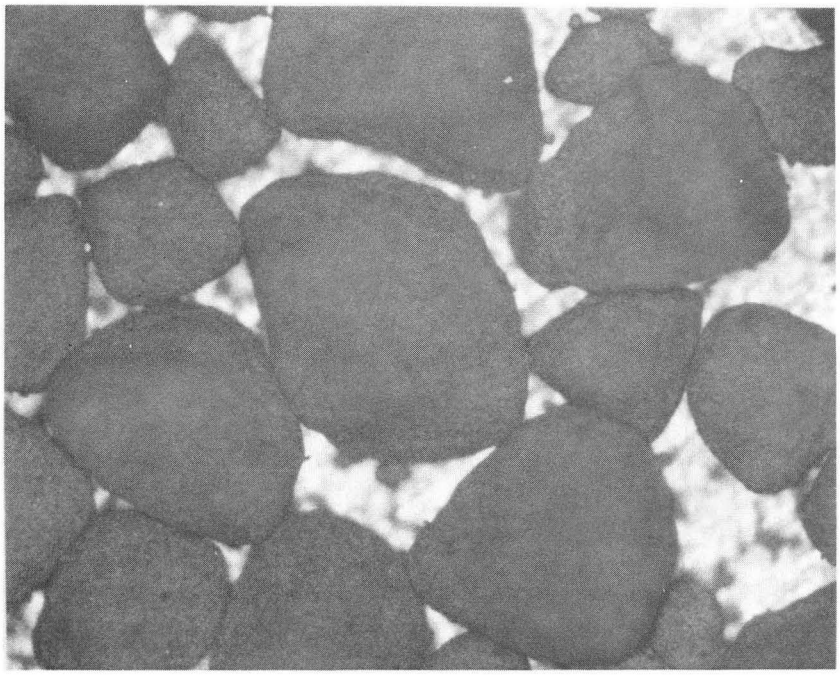

0.25 mm

Figure 2.2 Silicon carbide powder, as received.

1 μm

XBB 905-3841

Figure 2.3 Silicon carbide powder after mechanical grinding.

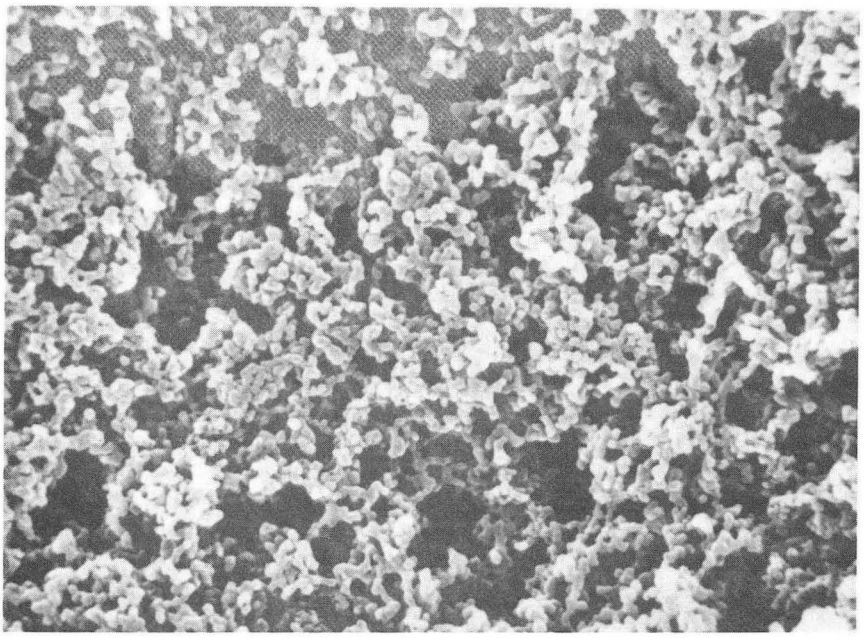

1 μm

Figure 2.4 Homogeneously precipitated PMMA.

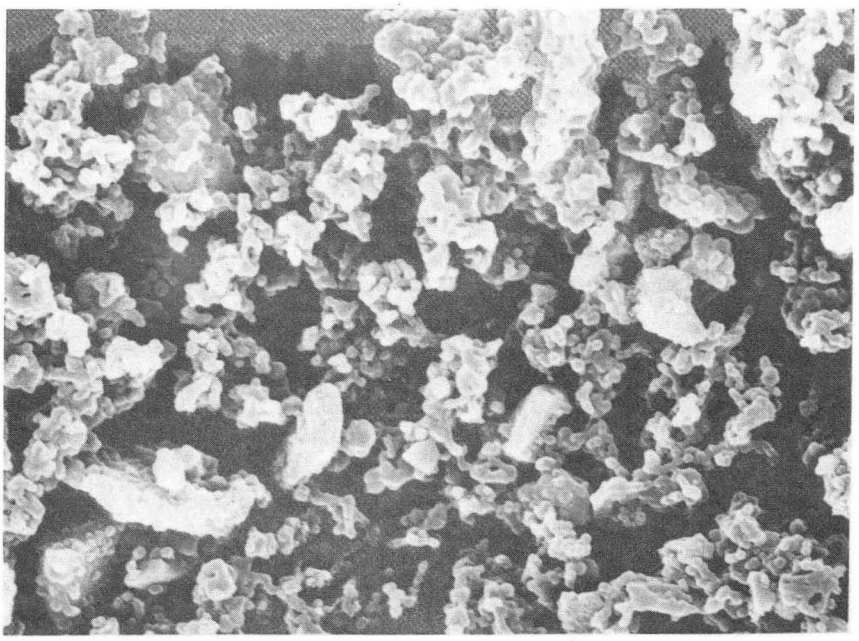

1 μm

XBB 905-3842

Figure 2.5 Results of initial encapsulation attempt.

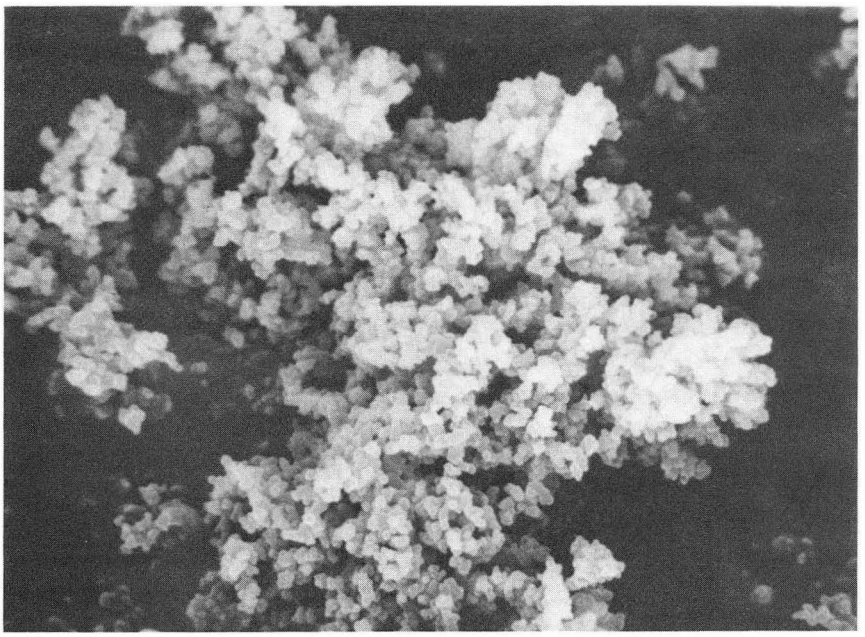

5 μm

Figure 2.6a PMMA encapsulated silicon carbide powder.

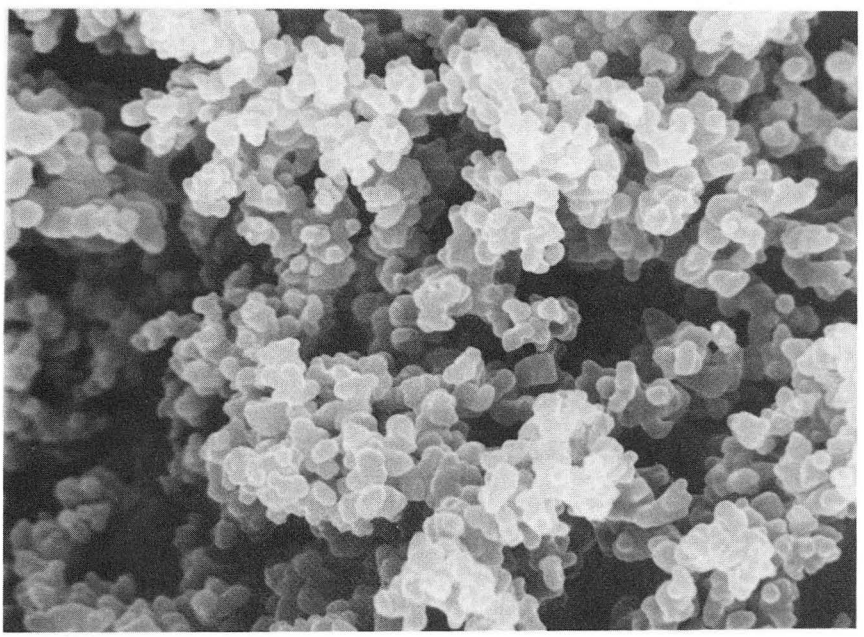

2 μm

XBB 905-3840

Figure 2.6b PMMA encapsulated silicon carbide powder.

occurring between coated particles, as was the case with homogeneously precipitated PMMA. TEM micrographs shown in Figure 2.7 allow measurements of the coating thickness to be made. As can be seen from these micrographs, the SiC-PMMA interface is continuous, which demonstrates conclusively that the polymer precipitated heterogeneously onto the surface, rather than homogeneously with subsequent agglomeration onto the substrates. The coating assumes a spherical configuration about the particle. The polymer coating varies in thickness from 0.1 μm at the particle corners to 0.3 μm along the faceted surfaces of the particles. Consistent with the nature of PMMA, the coating is completely amorphous, displaying no signs of crystallinity. Examination of powders from several encapsulation runs revealed that the coating thickness was easily controllable by varying the initial concentration of reactants. Similarly, the coating thickness was consistent when identical conditions are repeated.

2.6. Discussion

The encapsulation process was optimized by varying the concentration of reactants and nucleation sites within solution until a stable heterogeneous nucleation regime was reached. When reactant concentration is too high, uncontrolled homogeneous nucleation occurs in the bulk of solution, as illustrated by a LaMer diagram (Figure 2.8a). The monomer concentration profile is plotted versus time and the homogeneous and heterogeneous nucleation regimes shown. A reduction in homogeneous nucleation can be achieved by either decreasing the concentration of reactants by means of further monomer dilution, or by increasing the number of nucleation sites available. Further monomer dilution reduces the slope of the concentration profile (Figure 2.8b). By contrast, increasing the concentration of nucleation sites increases the consumption of monomer in the heterogeneous nucleation regime, thereby delaying or altogether suppressing homogeneous nucleation (Figure 2.8c).

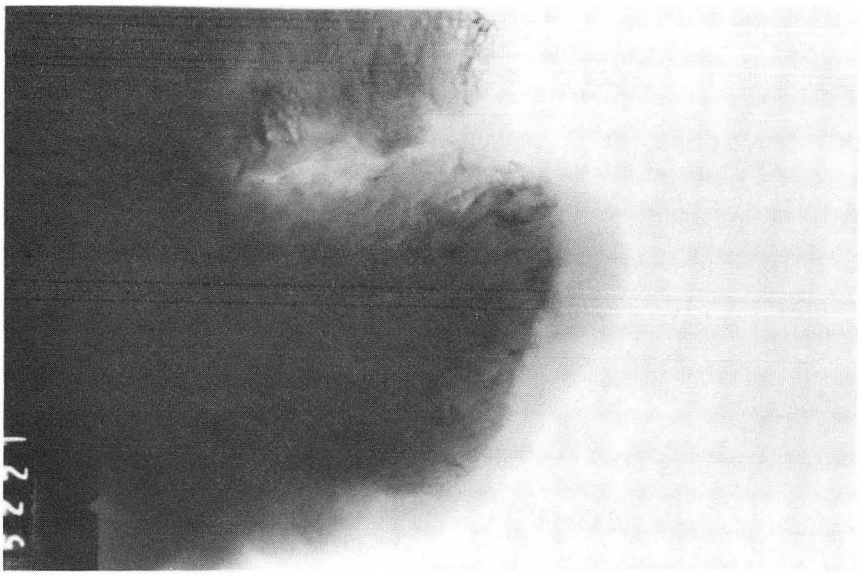

0.2 μm

Figure 2.7a TEM micrograph of SiC-PMMA interface.

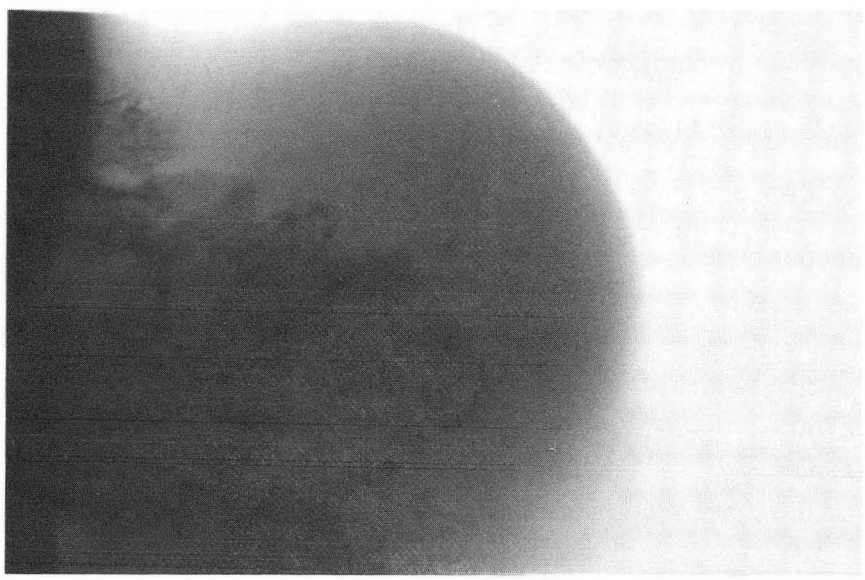

XBB 905-3839

0.1 μm

Figure 2.7b High magnification view of SiC-PMMA interface.

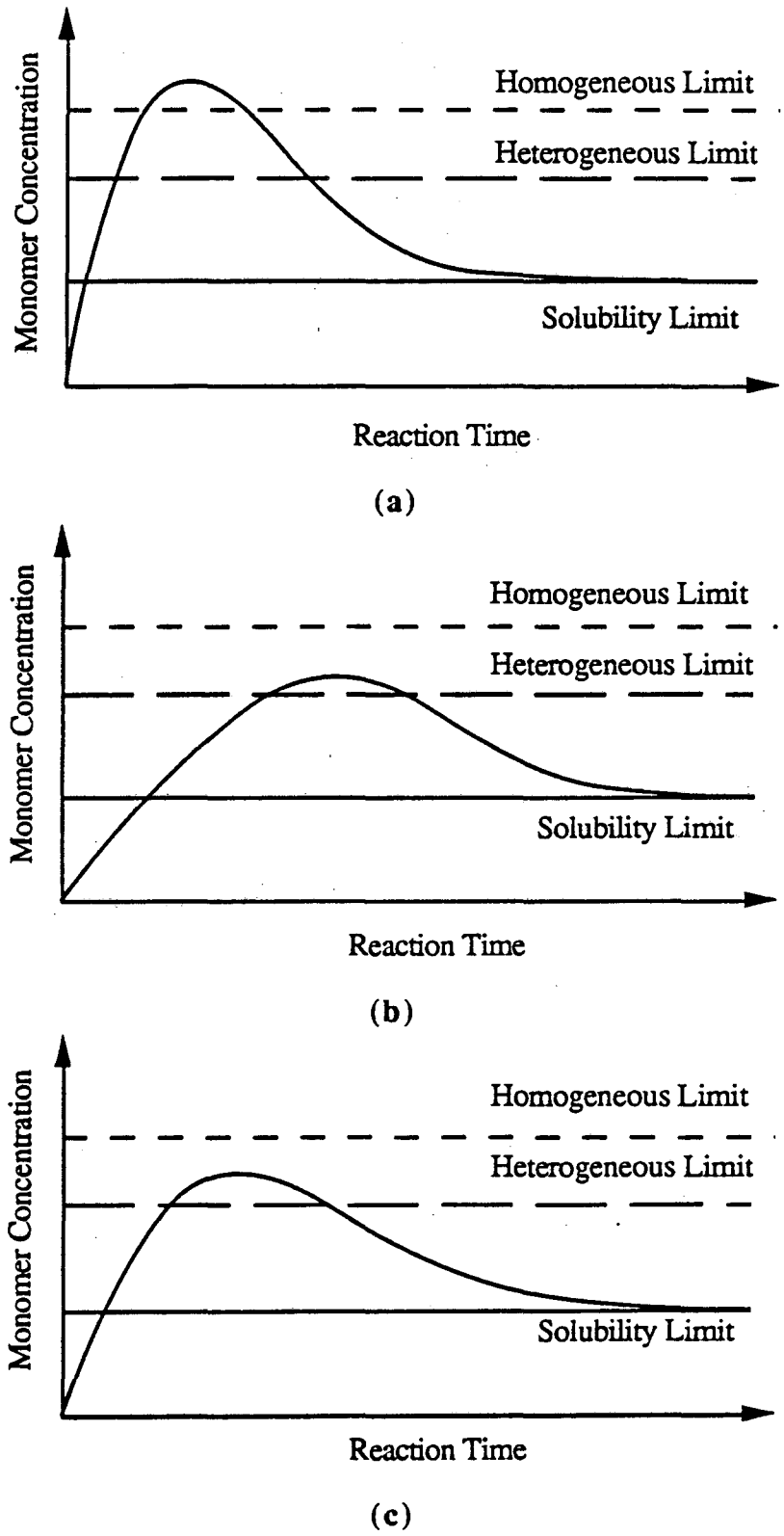

Figure 2.8 Effect of process variables on polymer nucleation.

In extremely dilute monomer solutions, the reaction concentration can be precisely varied, controlling the rate of polymer deposition, thus giving greater control over the coating thickness. Polymer loadings of 1.5-2% have been achieved,[39] where the polymer loading is defined as:

$$PL = \frac{wt\ of\ PMMA}{wt\ of\ PMMA + SiC} \tag{2.1}$$

By increasing the number of possible nucleation sites, however, much larger encapsulation runs can be achieved. Because of the relatively high polymer loading employed in this work, close coating thickness control was not required. Therefore, complete heterogeneous nucleation was achieved by first increasing the fraction of SiC in solution to near the suspension limit, followed by slowly decreasing the monomer concentration until the onset of homogeneous nucleation was suppressed.

The agglomeration of coated particles was observed, which is consistent with Coker.[39] He determined that inter-particle agglomeration began to occur at polymer loadings above approximately 3-6%. However, the critical polymer loading limit for agglomeration (PL_C) is dependent upon the specific nature of the polymer employed. For soft polymers, such as polyethyl acetate, PL_C will be lower, whereas for hard polymers, such as polymethyl methacrylate, PL_C will be substantially higher.

3. Crack Growth Behavior of Particulate Composites

Many investigations have been undertaken to study the sensitivity of particulate composites to pre-existing flaws. Several theories have been developed to explain the various effects of second phase particles on the toughness of particulate composites. The following is a brief overview of these theories.

3.1. Crack Pinning

One of the earliest theories on the fracture toughness of particulate composites was proposed by Lange.[42] By analogy to dislocation theory, it was reasoned that a crack front will have a line energy. Thus, any increase in line energy caused by interactions with second phase particles will influence the toughness of the composite. When a crack front encounters a row of second phase particles, the front becomes pinned. As the applied stress increases, the crack front will bow out between the particles (Figure 3.1a). Calculations show that the stress (σ_A) required to propagate a crack through the particles is related to the line tension (T) by:[42]

$$\sigma_A^2 = \frac{2E}{\pi C'}\gamma, \quad where \;\; \gamma = \gamma_o + \frac{T}{2C} \tag{3.1}$$

where C' is the primary flaw or crack size, E is the Young's modulus, γ is the fracture surface energy, γ_o is the surface energy of the un-reinforced matrix, and $2C$ is the interparticle spacing. The crack is assumed to break away when two adjacent crack segments meet. This breakaway condition occurs when the crack segments reaches a semi-circular configuration (Figure 3.1b), at which point the line tension is given by:

$$T = \frac{2}{3}C\gamma_o \tag{3.2}$$

Evans has extended this approach to a semi-elliptical crack configuration and non-spherical pinning particles.[43] He demonstrated that the breakaway configuration corresponds to a semi-circular crack front only under very specific conditions. At all other times, the crack front profile is semi-elliptical at breakaway (Figure 3.1c).

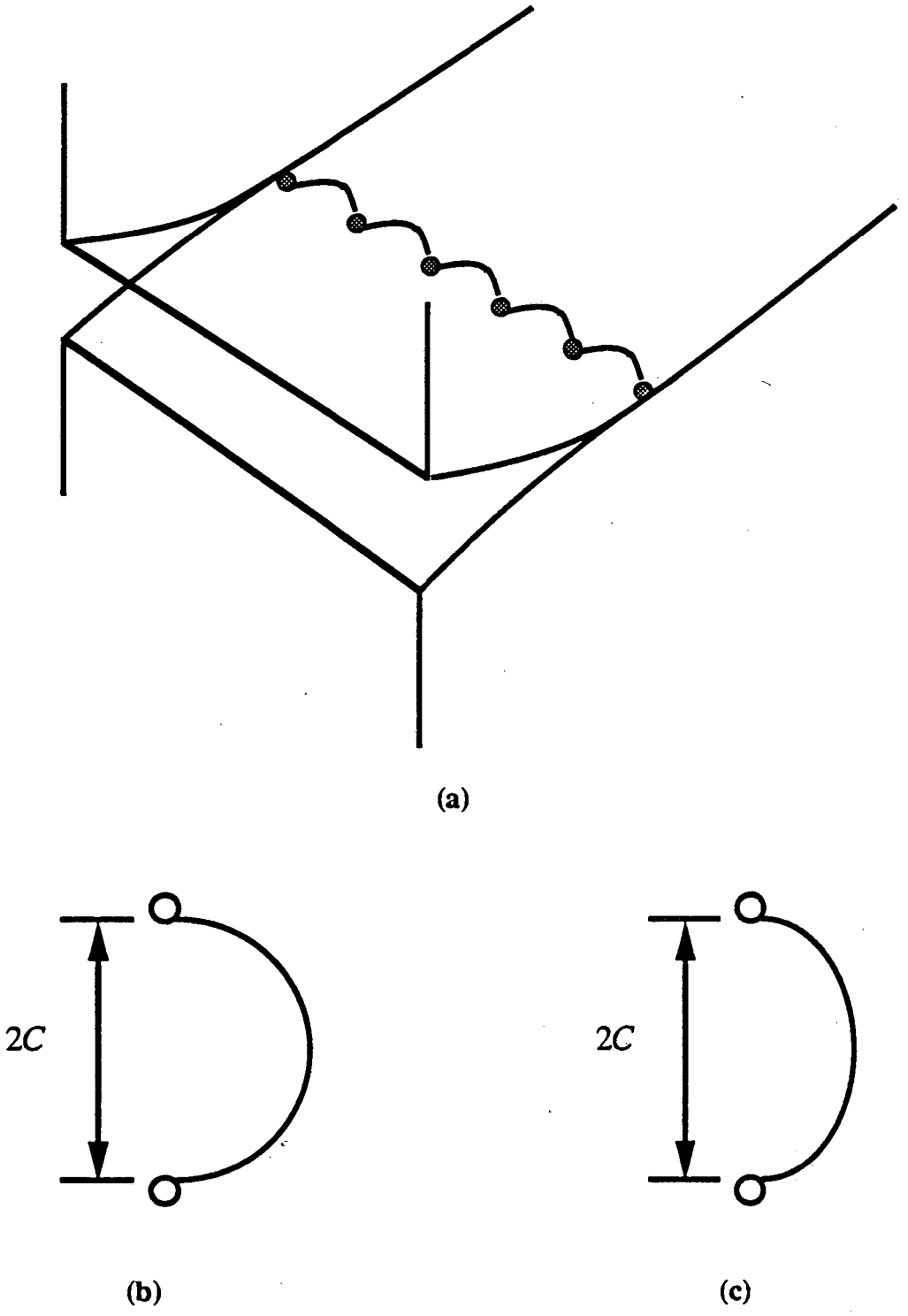

Figure 3.1 Schematic representation of crack pinning.

The line tension effect has also been examined for differing conditions of initial flaw size C' versus interparticle spacing $2C$.[43] Calculations reveal that line tension has a profound effect on the toughness of brittle matrix composite when C' is much greater than $2C$. For C' less than $2C$, there is no contribution to toughening from line tension. In fact, as the particles are crack initiating flaws, the toughness may be degraded. Finally, when C' is on the order of $2C$, the effect of line tension is not immediately apparent, and depends on the system considered.

Acoustic emissions techniques (AE) have been applied to study the effect of crack pinning in sand-polyester and sand-clay-polyester composites.[44] A low fracture toughness was observed in sand-clay-polyester composites due to the embrittlement by the clay particles. This embrittlement was observed to decrease crack pinning effectiveness, and was substantiated by the short, continuous nature of the AE response. In addition, the fracture surface showed a quasi-cleavage failure mode, confirming the AE data. By contrast, sand-polyester composites showed relatively high fracture toughness, with a discontinuous AE response consistent with the stepwise fracture surfaces observed. Substantial evidence therefore exists that suggests that crack pinning may strongly influence the fracture toughness of particulate composites.

Work by several researchers have shown that the optimum fracture toughness reinforcement of the polymer matrix is related to the particulate loading, with the optimum occurring between 20 and 30 vol% particulates.[12,45-47] An explanation for this phenomenon has been suggested by Lange[48] and supported by Mallick.[12] Again, according to Lange, the fracture energy/unit area of a composite is given by:

$$\gamma = \gamma_o + \frac{T}{2C} \tag{3.3}$$

where γ_o is the fracture surface energy of the unfilled matrix, T is the critical line tension of the crack front, and $2C$ is the distance between pinning positions. This expression assumes a semi-circular critical crack front with idealized 0-dimensional pinning points.

As the particulate volume fraction increases, the inter-particle spacing decreases, thus increasing the curvature of the crack front.[49] A smaller crack front arc requires that greater force be applied to break the crack away from the pinning points.

It was concluded that beyond the optimum volume fraction of particles, the force required for the crack front to break away from the pinning points is so great that the particle-matrix interface debonds.[50] As the volume fraction increases, the crack advances in ever smaller steps until the discontinuous fracture mode is replaced by a continuous one. At this point, the fracture energy/unit area becomes the energy/unit area of the matrix plus the energy required to debond the particle-matrix interface.

In addition to particulate loading, the size of particulates also has a significant effect on the fracture toughness of composites. This can be rationalized by considering the effectiveness of the pinning points constraining the crack front.[48] As seen previously, the fracture energy/unit area (γ) depends upon the size of the crack front arc. However, γ should also depend upon the shape of the crack front, which is in turn related to the effectiveness of the pinning points constraining the crack. Therefore, the hypothesis is that the overlap of stress fields from adjacent crack fronts determines the final crack front shape. For smaller pinning points, the stress overlap is reduced and therefore the amount of crack front bowing is decreased (Figure 3.2a). The result is a decrease in the effectiveness of the pinning points. For larger pinning points, the bowing will be greater (Figure 3.2b). For a finite pinning size d, a dimensionless function $f(d)$ is introduced to the second term of equation 3.3 to account for this condition,

$$\gamma = \gamma_o + f(d)\frac{T}{2C} \tag{3.4}$$

where $0 \leq f(d) \leq 1$. When $f(d) = 0$, there is no contribution to toughness from line tension effects since there is effectively no pinning present. When $f(d) = 1$, the pinning causes the crack front to bow out to a semi-circular critical condition.

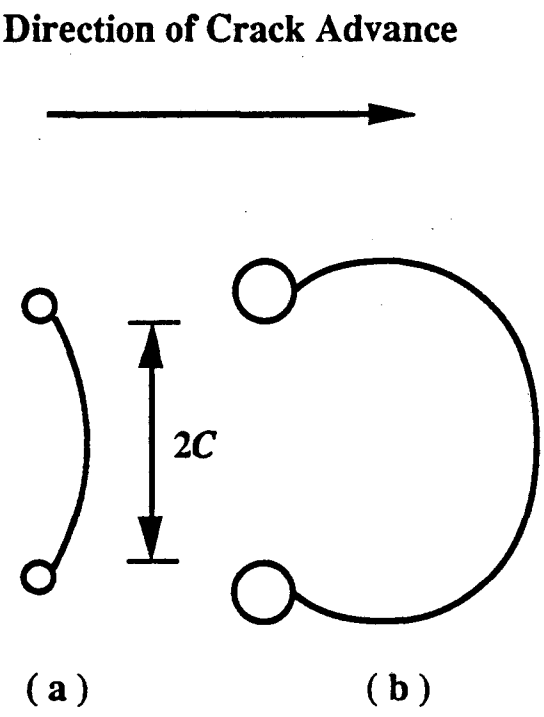

Figure 3.2 Effect of particle size on crack front bowing.

3.2. Crack Deflection

Crack deflection processes are effective in enhancing the toughness of particulate composites.[51] As the reinforcing phase deflects the crack front away from the Mode I loading condition, a Mode II component is introduced. This is schematically shown in Figure 3.3. As the crack front moves away from Mode I loading, a decrease in the local stress intensity (K_{Tip}) near the crack tip develops. By reducing K_{Tip}, the driving force for crack advance diminishes, thereby toughening the material. When crack deflection mechanisms are in operation, the driving force reduction should be equal throughout the entire range of crack growth rates. The magnitude of the reduction is dependent only upon the volume fraction and shape of the reinforcing phase.[52]

3.3. Crack Tip Shielding

The theories of crack pinning and crack deflection are derived from 2-dimensional models of the crack front. More recently, however, interest has focused on the 3-dimensional effect of a crack front on the surrounding matrix process zone. Evans has treated this topic for polymer composites in terms of matrix debonding and microcracking/crazing.[31] Although these processes are mechanistically different, the development of the process zone remains fundamentally the same.

The theory of toughening by process zone shielding depends upon the non-linear stress-strain response in the matrix material. This is easily visualized when the non-linear deformation mechanisms in polymers are considered . Polymers generally deform by crazing at ambient temperatures.[53] When a second phase particle is present, the process of debonding at the particle-matrix interface is introduced, with the amount of debonding naturally dependent upon the strength of the interface. Additionally, microcracking or crazing between closely spaced particles may occur. This is likely to occur when significant misfit strains are present. The strains result from residual stresses in the matrix caused by thermal expansion mismatch between the two phases.[30] For the purposes of this

analysis, only the mechanism of interfacial debonding will be considered, although the same analysis would apply to any of the processes mentioned.

3.3.1. Frontal Process Zone

Ahead of the tip of the crack lies the frontal process zone (Figure 3.4a), a region that has experienced continuous straining as a result of the applied stress, with no strain reversal. Within this region, the material has debonded and it's Young's modulus has decreased from E to E_1. The stress intensities are related by:[31]

$$\frac{K_{\infty}^2}{E} \approx \frac{K_{Tip}^2}{E_1} \tag{3.5}$$

from J-integral path-independence. Since $E_1 < E$, there is a reduction in K at the crack tip during debonding, resulting in crack tip shielding. However, degradation of the material is also occurring in this zone, reducing the local crack propagation resistance (K_C^M). Assuming that the debonded region can be modelled as a porous medium,

$$K_C^M \approx K_C(1 - f_S) \tag{3.6}$$

where f_S is the volume fraction of debonded particles at saturation, and K_C is the toughness of the base material. Therefore, the measured toughness of the debonded composite is given by:

$$K_C^{\infty} \approx \sqrt{\frac{E}{E_1}}(1 - f_S)K_C \tag{3.7}$$

Furthermore, since the ratio E_1/E is given by f_S, the measured toughness is only a function of f_S.

3.3.2. Process Zone Wake

As the crack advances through the frontal process zone, a process zone wake develops (Figure 3.4b). This wake provides the second contribution to crack shielding.

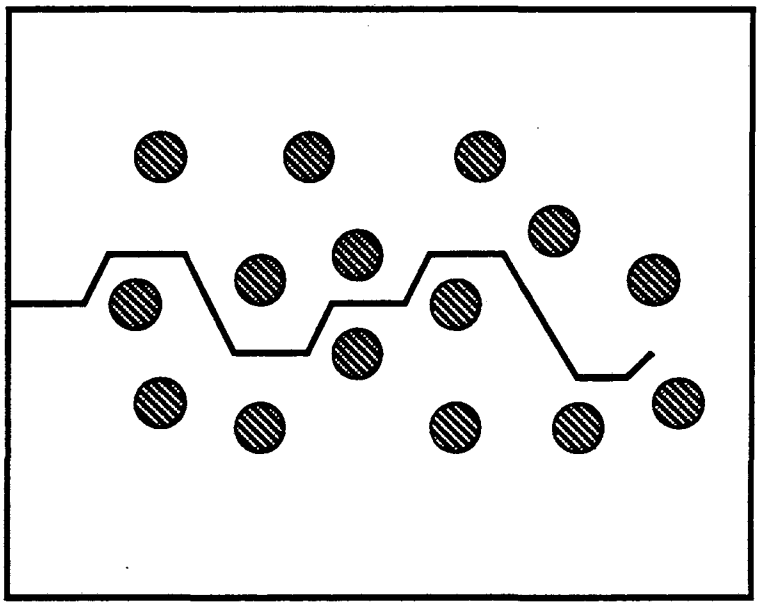

Figure 3.3 Crack deflection.

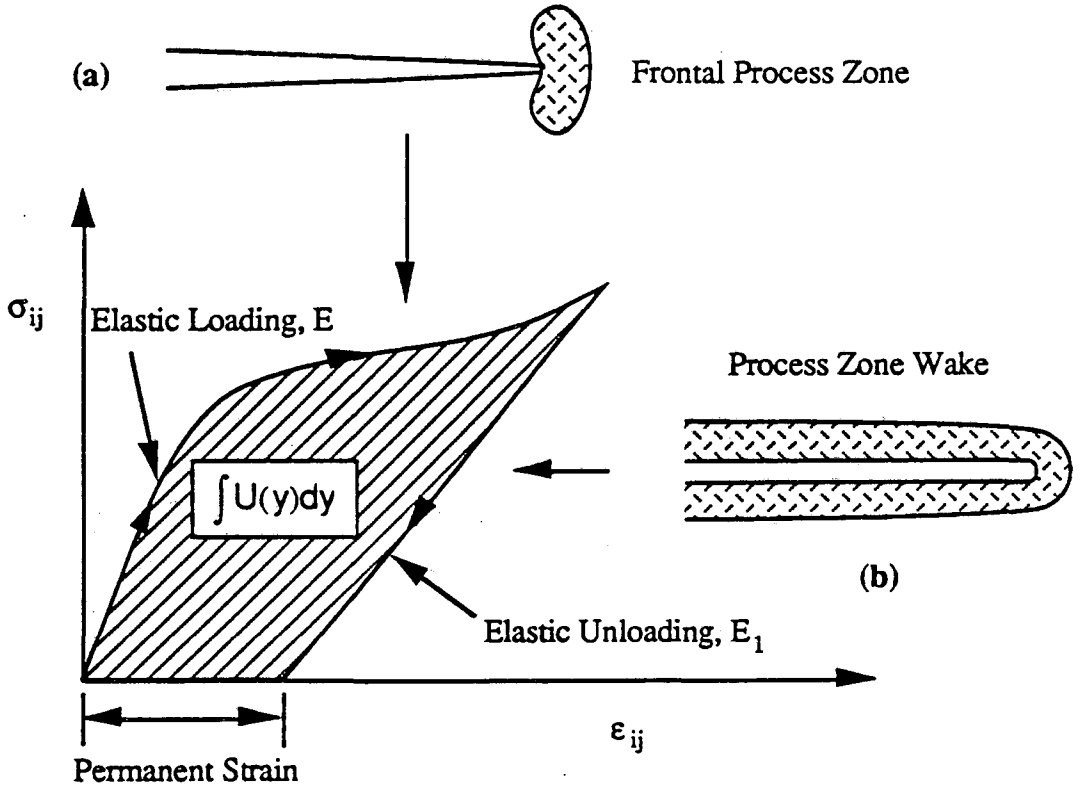

Figure 3.4 Process zone shielding due to non-linear stress-strain response.

Within this process zone wake, the material has undergone an unloading cycle, and for a steady-state wake, the measured toughness is given by:[31]

$$\frac{K_{\infty}^{2}}{E}=\frac{K_{Tip}^{2}}{E_{1}}+2\int_{0}^{h}U(y)dy \tag{3.8}$$

where $U(y)$ is the residual energy density, and h is the process zone height. The factor of two in the term accounts for the two halves of the crack front. The residual energy density is given by the area under the stress-strain curve. This is evident as the material in the wake has experienced a complete stress-strain cycle due to crack advance, with an associated permanent dilation of material in the wake. The total crack shielding has been calculated by Evans:[54]

$$K_{C}^{\infty}\approx K_{C}(1-af_{s})+bEf_{s}\sqrt{h}\theta \tag{3.9}$$

where a and b are constants, and θ is the permanent dilation resulting from interfacial debonding.

3.4. Crack Bridging Mechanisms

Crack bridging has also been reported as a significant toughening mechanism for brittle composite materials.[55] Toughening occurs because the uncracked material in the crack wake acts as an impediment to crack opening. This impediment reduces the applied stress at the crack tip, thus enhancing the resistance of the material to fracture. For the case of a brittle second phase, two possible mechanisms exist.

3.4.1. Co-planar Uncracked Ligaments

The first mechanism involves the existence of uncracked ligaments which exist in the plane of the crack (Figure 3.5a). Modelling of this condition has been undertaken by means of a limited crack-opening displacement approach.[32] For this approach, the stress in a ligament behind the crack tip is assumed to be related to the crack opening at that point. Crack advance is therefore limited by the crack-opening displacement constraint imposed

by the ligament. The point of ligament breakage corresponds to the critical crack opening displacement, which varies with the area fraction of ligaments f, but is independent of the size of the bridging zone. Calculations lead to an expression for the degree of crack-tip shielding due to uncracked ligaments (K_S):[32]

$$K_S = -fK_a \frac{(1+F)^{\frac{1}{2}} - 1}{1 - f + f(1+F)^{\frac{1}{2}}} \tag{3.10}$$

where K_a is the applied stress intensity, and F is a function of the ligament geometry.

In studies of Al/SiC metal matrix composites, Shang has determined that the contribution to shielding by co-planar uncracked ligaments is on the order of 6%, a minimal increase.[56]

3.4.2. Overlapping Crack Ligaments

The second mechanism for crack bridging involves the formation of ligaments by overlapping cracks (Figure 3.5b). For overlapping ligaments, the crack-tip shielding limit is not due to the critical crack-opening displacement, as is the case for co-planar ligaments, but rather to the strength of the ligament. In this case, a limiting strain approach is more appropriate for the analysis of the degree of crack tip shielding provided by the overlapping ligaments.[32] The limiting strain approach assumes that the bridges are composed of tensile ligaments, where the stress is proportional to the ligament strain. The limiting fracture strain is therefore experienced by the last ligament in the bridging zone, and thus defines the length of the zone. Such calculations lead to an expression for K_S:[56]

$$K_S = -f\sigma_y \frac{2\sqrt{2l}}{\pi}\left\{1 + \frac{k}{\sigma_y}\left[\ln(1+F) + 2\left(\sqrt{1/F}\tan^{-1}\sqrt{F} - 1\right)\right]\right\} \tag{3.11}$$

where l is the length of the bridging zone, σ_y is the yield stress of the ligaments, k is a constant, and all other variables as defined previously.

Again, for overlapping ligaments in Al/SiC metal-matrix composites, Shang has found the contribution to toughening to be on the order of 30% or more.[56] Such

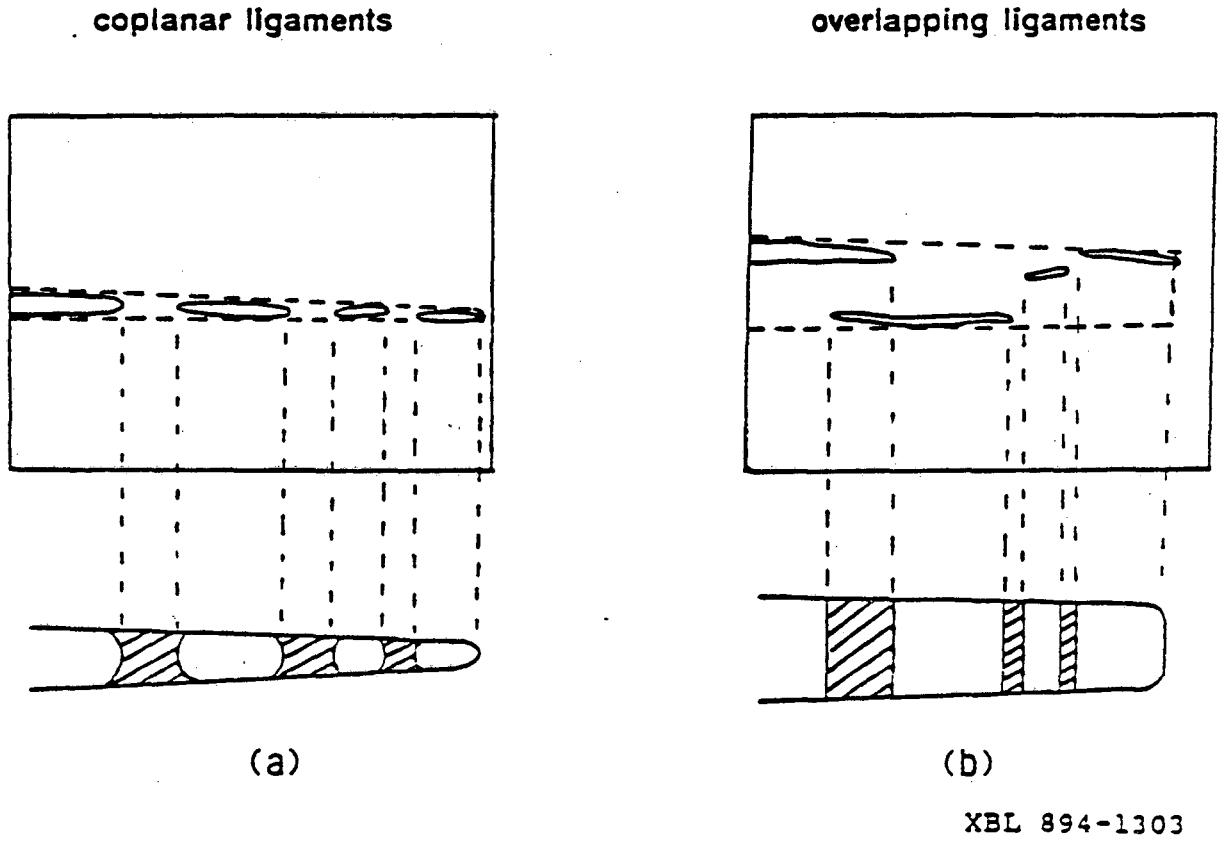

Figure 3.5 Schematic illustration of uncracked ligament bridging from a) co-planar and b) overlapping ligaments (after Shang[56]).

calculations lead to the conclusion that crack bridging by overlapping ligaments is a substantially more potent form of crack shielding than co-planar uncracked ligaments.

3.5. Experimental

Following the optimization of the encapsulation process, composites of different particle sizes ranges were formed by die pressing the powder above the glass transition temperature (T_g) of PMMA. The silicon carbide loading was chosen to be 30 volume percent. The volume fraction of silicon carbide was determined by polymer burnout measurements. For mechanical property comparison purposes, composite samples of this loading were also prepared using a conventional casting technique. One sample of each condition was tested for fatigue and fracture propagation resistance.

3.5.1. Encapsulation Processed Composite Forming

Encapsulation processed silicon carbide powder of size ranges 1, 16, and 100 μm were die pressed to form the composite. A schematic representation of the press is shown in Figure 3.6. A quantity of encapsulated powder was placed in a 1" diameter die press, and a pressure of 27 MPa applied. While under pressure, the powder was heated to 150°C. The temperature employed was slightly above the glass transition temperature of PMMA to overcome any changes in T_g due to the presence of a second phase in the composite.[57-59] Heat and pressure were maintained for 20 minutes, followed by water jacket cooling for an additional 20 minutes. The pressure was then released and the finished pellet carefully removed from the press.

3.5.2. Conventional Composite Casting

The as-received silicon carbide powders were prepared as described in section 2.3. A measured quantity of methyl methacrylate was poured into a small container. One wt% benzoyl peroxide (initiator) and 0.03 vol% N,N-dimethyl p-toluidline (accelerator) were

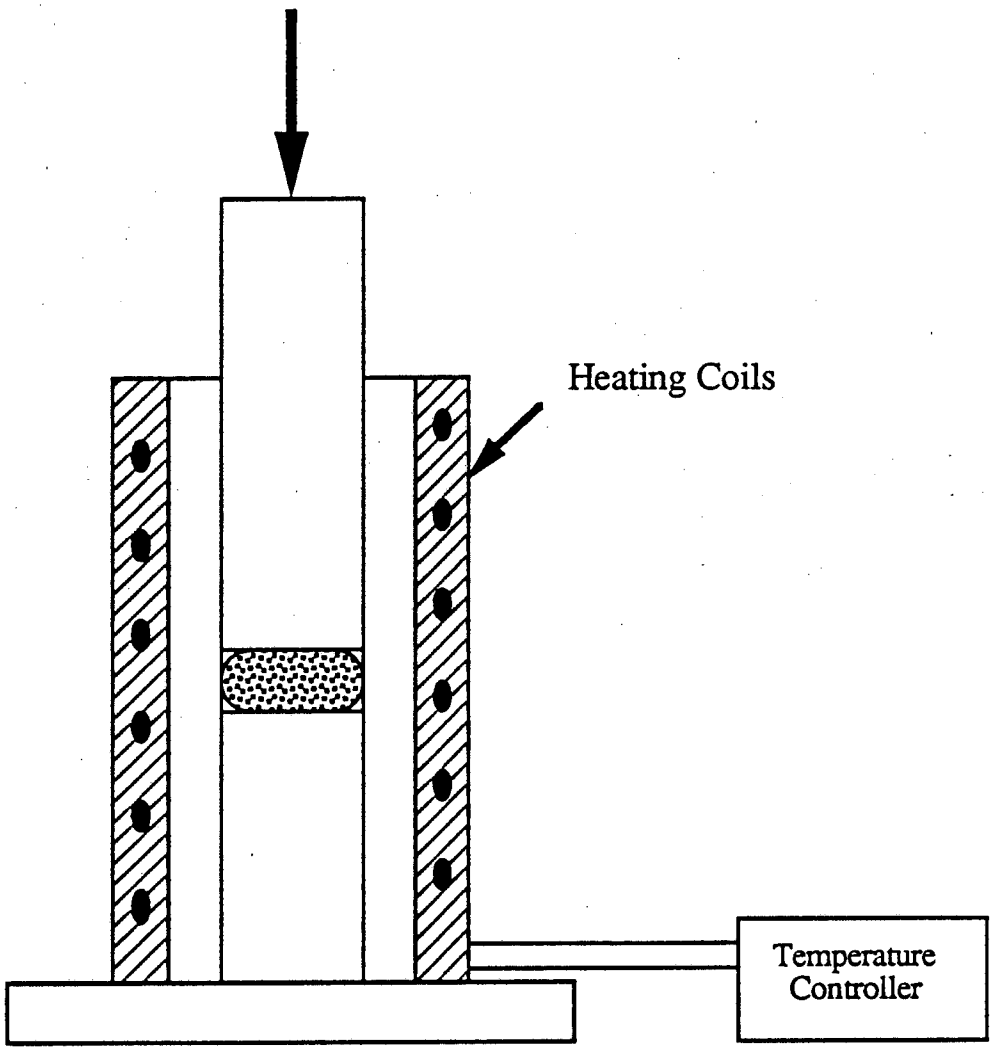

Figure 3.6 Schematic illustration of the pressing apparatus.

added. Because of the volatile nature of the reactants, the container was capped to prevent evaporation during reaction.

When the viscosity of the polymerizing system increased sufficiently to prevent any subsequent settling of the particles (one to two hours), the silicon carbide was incorporated and stirred vigorously for maximum dispersion. The mixture was then poured into 1" diameter greased rings placed on a glass plate and allowed to set. The molds were cured at 110°C for one hour to complete the polymerization process.

3.5.3. Subcritical Crack-Growth Testing

Fracture toughness samples were machined to form disc-shaped compact tension specimens following the specification of Figure 3.7. Typical dimensions include a specimen width (W) of 17.5 mm, thickness (B) of approximately 2 mm, and an initial notch length of 11.5 mm. The radially edge-cracked disc configuration has been shown to be very effective for the testing of PMMA, compared to other standard geometries.[60] After machining, the specimen faces were polished so that crack profile detail can be more easily seen.

Cyclic fatigue-crack propagations rates (da/dN) were determined by the method developed by Dauskardt and Ritchie,[29] in general accordance with the current ASTM Standard E647-86A for *Measurements of Constant-Load Amplitude Fatigue Crack Growth Rates*. Crack growth rates were determined using the linear-elastic fracture mechanics approach, in terms of the stress-intensity (K) for monotonic loading conditions, and stress-intensity range (ΔK) under cyclic loading conditions. The stress-intensity is defined as:

$$K = Q\sigma\sqrt{\pi a} \tag{3.12}$$

where σ is the applied stress, a is the crack length, and Q is a geometric factor on the order of unity. The stress-intensity range (ΔK) is given by:

$$\Delta K = K_{MAX} - K_{MIN} \tag{3.13}$$

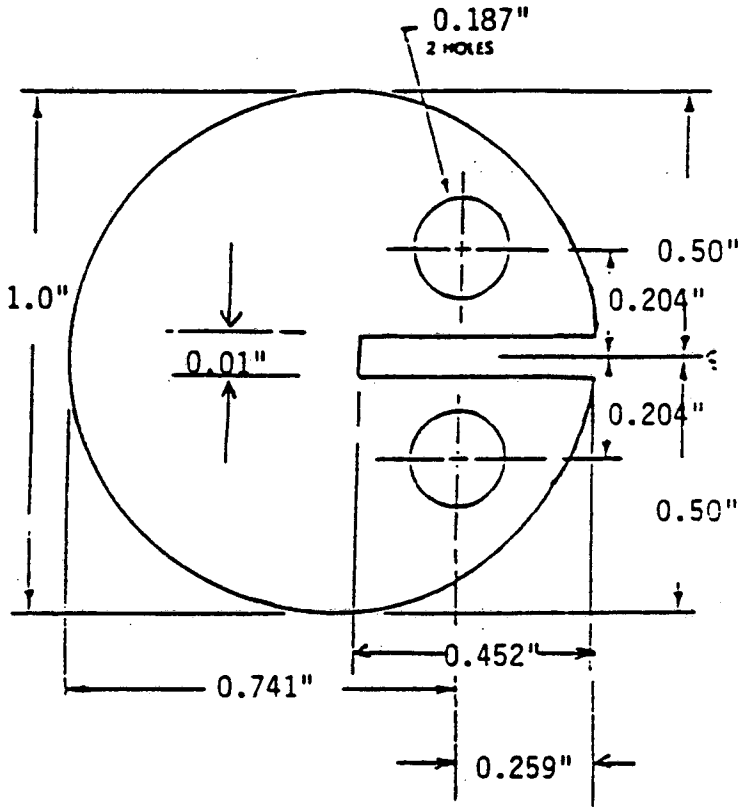

Figure 3.7 Disc-shaped compact tension specimen specifications.

Testing was performed using an electro-servo-hydraulic testing system incorporating an MTS 831 load frame, an MTS 458 MicroConsole controller, and an IBM PC/AT with high speed data acquisition card (100kHz sampling rate). Tests were carried out under either closed-loop displacement or stress-intensity control.

Fatigue-crack propagation tests were performed at controlled room temperature (22°C) at a sinusoidal frequency of 50 Hz and a load ratio R (ratio of minimum to maximum loads) of 0.1. The threshold stress intensity range below which, crack growth is presumed dormant (ΔK_{TH}), was defined at growth rates below 10^{-11} m/cycle, following ASTM E647 standard procedure. Under computer-control, thresholds were approached by varying the applied loads so that the instantaneous values of crack length (a) and stress intensity (K) varied according to:

$$K = K_o \exp\left[C^*(a - a_o)\right] \tag{3.14}$$

where a_o and K_o are the initial values of a and K, and C^* is the normalized K-gradient ($1/K \cdot dK/da$), set to -0.09 per mm of crack extension.

Stress intensity values were computed from handbook solutions for the test geometry in terms of the applied load (P) and crack length (a) as:

$$K = \left(P / BW^{\frac{1}{2}}\right) \cdot f(a/W) \tag{3.15}$$

where:

$$f(a/W) = \frac{(2 + a/W)\left(0.76 + 4.8a/W - 11.58(a/w)^2 + 11.43(a/W)^3 - 4.08(a/W)^4\right)}{(1 - a/W)^{\frac{3}{2}}} \tag{3.16}$$

Crack initiation was achieved by machining a wedge-shaped starter notch of approximately 2 mm in length, from which a fatigue crack was grown under displacement control.

Crack propagation rates (da/dN) were continuously monitored by means of a d.c. electrical-potential gauge.[61] Thin (20 μm) Ni-Cr metal foils were bonded to the specimens

and the changes in electrical potential across the crack (at constant current) monitored by test equipment. The digital output was relayed to the computer for control and data processing, while the analog output was displayed on a strip-chart recorder to provide continuous monitoring of crack extension (Figure 3.8). Crack-growth rates were determined by numerical differentiation of measurements of crack length (a) from the Ni-Cr foil as a function of the number of cycles (N). The data is presented on a standard log-log graph of crack growth rate (da/dN) as a function of the stress intensity range (ΔK).

3.5.4. Fracture Toughness Measurements

Following completion of the subcritical crack-growth test, the fracture toughness (K_c) was determined under displacement control. The resistance-curve (R-curve) behavior from specimens containing a fatigue pre-crack was analyzed according to ASTM Standard E399-87 for the *Plane Strain Fracture Toughness of Metallic Materials*. Values of the fracture toughness were defined at crack initiation (K_{Ii}) and at the steady state plateau (K_{Ic}) on this curve. The data is presented on a linear-linear graph of stress intensity (K_I) as a function of differential crack extension (Δa).

3.6. Results

Large shrinkage stresses leading to severe cracking were observed in sample 1C.* Cracking was observed to occur before the curing stage. The shrinkage was estimated to be on the order of 20%. This behavior was not observed in any other cast sample. No test data results were therefore available from this particle size/processing combination. Sample 16C failed catastrophically during fatigue testing. As R-curve behavior is tested following fatigue testing, no data was available.

---

* A note on nomenclature: each sample is identified by a number representing the particle size of reinforcement (1, 16, 100 μm), and a letter designating the method of processing (P - encapsulation processed, C - conventionally cast).

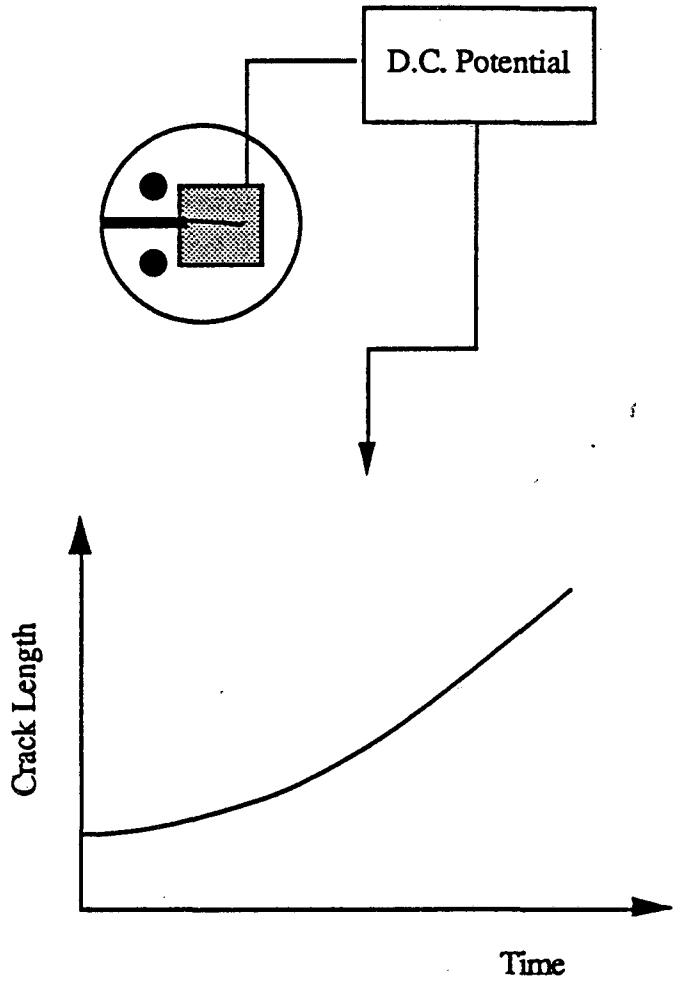

Figure 3.8 Crack length measurement by d.c. potential gauge.

3.6.1. Crack-Growth Rates

The fatigue crack-growth rates (da/dN) for series P (Figure 3.9) and series C (Figure 3.10) are plotted as a function of the stress intensity range (ΔK) for $R = 0.1$. The growth rates span three orders of magnitude from 10^{-11} to 10^{-9} m/cycle, over a range of ΔK from 0.3 to 1.1 MPa(m)$^{1/2}$. The data for each sample follow a conventional Paris law relationship, similar to that for metals:[62]

$$da / dN \propto (\Delta K)^m \tag{3.17}$$

With the exception of sample 16C, each sample displayed an apparent fatigue threshold, below which the crack is assumed dormant. The fatigue threshold is determined by decreasing ΔK until crack growth is arrested. Since sample 16C did not approach threshold, catastrophic failure occurred. The measured values of stress intensity range at threshold (ΔK_{TH}) ranged from 0.36 to 0.71 MPa(m)$^{1/2}$.

When the data points from the two series are overlaid (Figure 3.11), it is clear that fatigue-crack propagation occurs over a relatively narrow range of ΔK. Especially good agreement exists between the sample 100P and sample 100C growth rates, while the crack growth behavior for sample 1P is noticeably inferior.

3.6.2. Fracture Toughness

Fracture toughness (K) data obtained from R-curve tests are presented in Figure 3.12, plotted against crack extension (Δa). The toughness values defined at initiation (K_{Ii}) and plateau (K_{Ic}) are displayed in Table II. Fracture toughness data for sample 16C was not available as catastrophic failure occurred during fatigue cycling. The measured toughness ranged from 0.69 to 2.37 MPa(m)$^{1/2}$ at K_{Ii} and from 0.71 to 2.95 at K_{Ic}. The toughness was observed to increase with increasing particle size, and sample 100P superior to 100C.

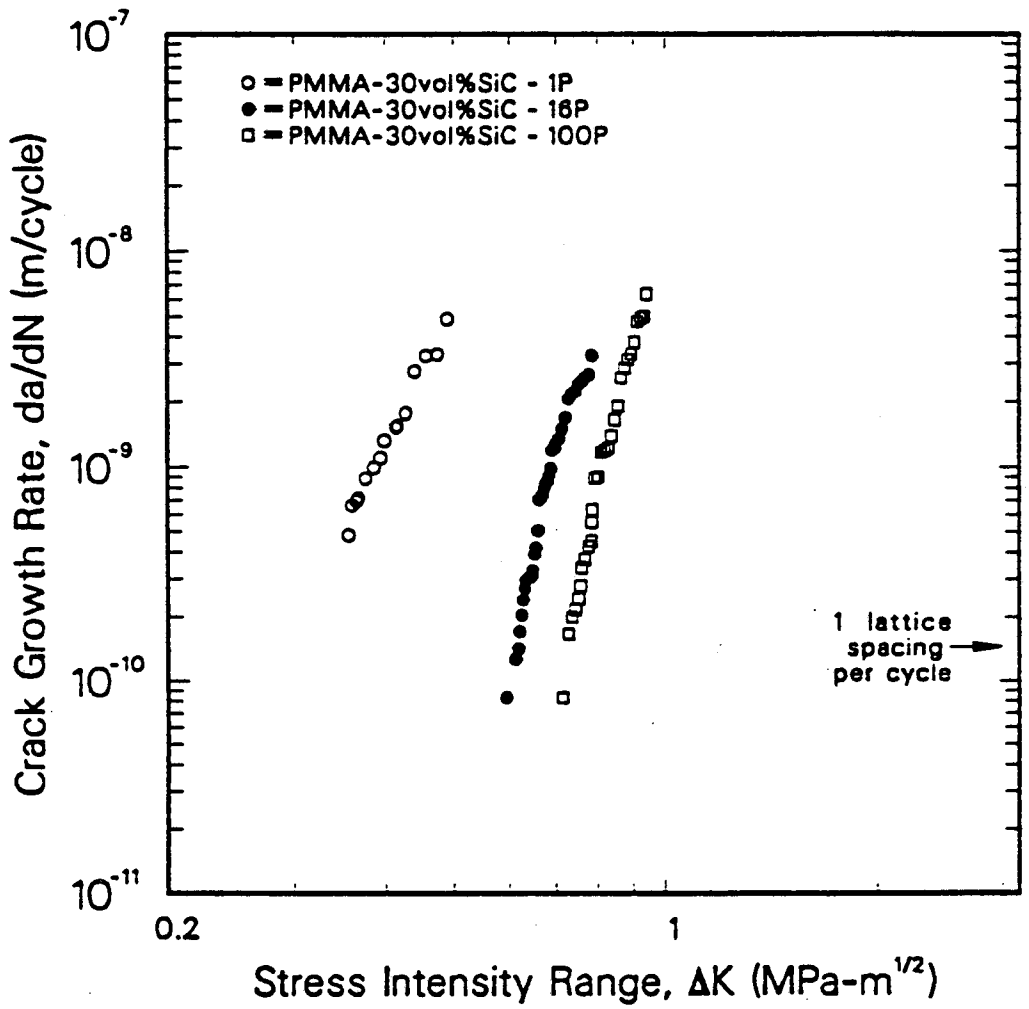

Figure 3.9 Fatigue crack growth rates for series P composites.

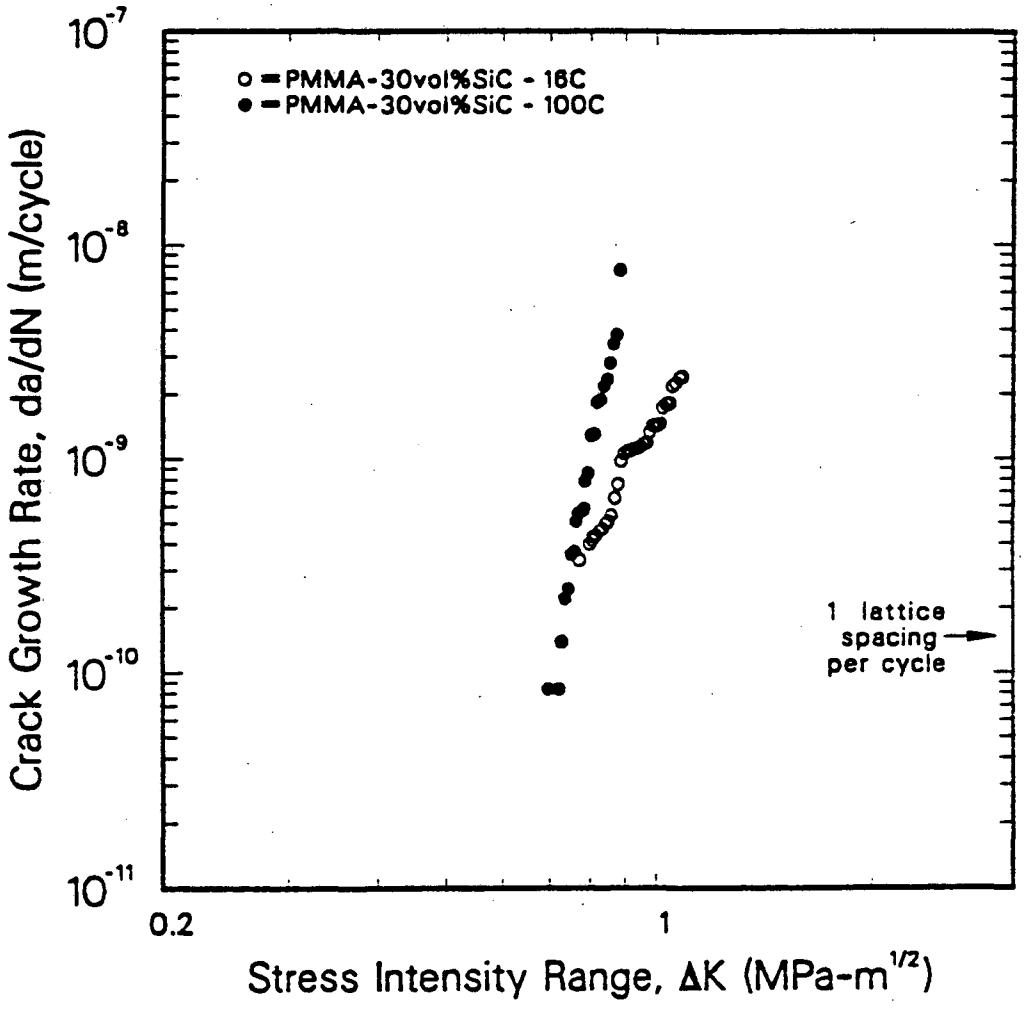

Figure 3.10 Fatigue crack growth rates for series C composites.

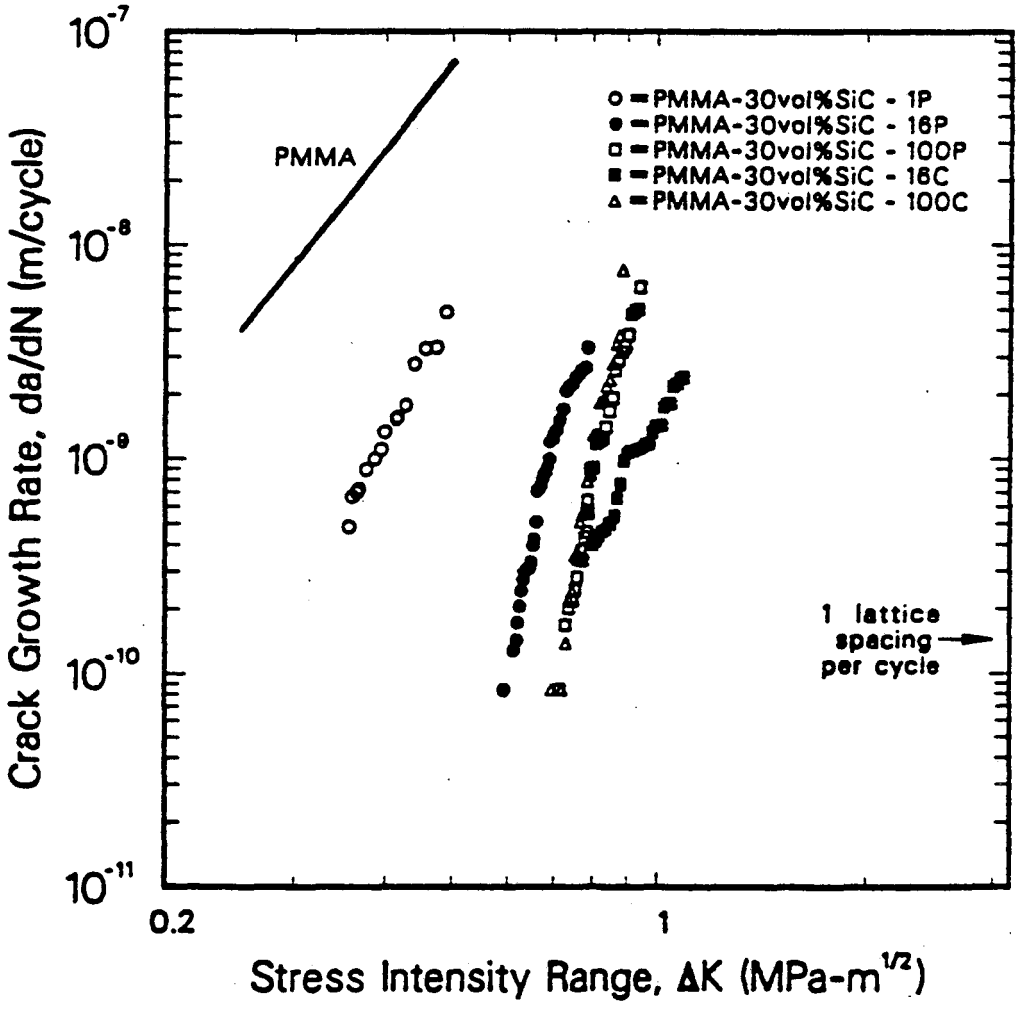

Figure 3.11 Fatigue behavior for series P and C composites. Unreinforced PMMA shown for comparison.[53]

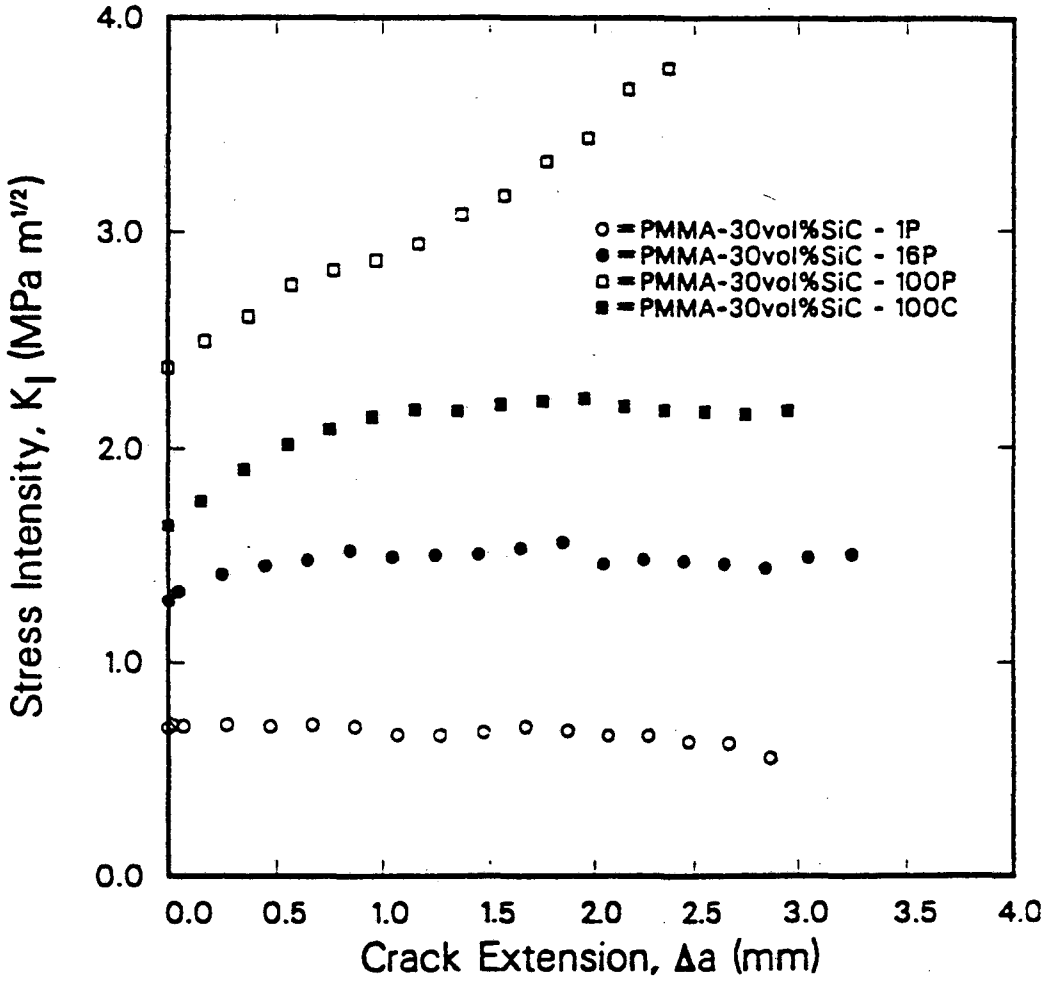

Figure 3.12 *R*-curve behavior for series P and C composites.

Sample:	K_{Ii} (MPa(m)$^{1/2}$)	K_{Ic} (MPa(m)$^{1/2}$)
1P	0.70	0.71
16P	1.29	1.50
100P	2.37	2.95*
100C	1.64	2.22

* Extrapolated value

Table II Measured values of fracture toughness at K_{Ii} and K_{Ic}.

The K_{Ic} value for sample 100P was extrapolated, as the sample displayed unusual *R*-curve behavior. No steady state plateau was observed, although an onset can be seen. The sustained increase in stress intensity (K_I) with increasing crack extension (Δa) is likely due to a large-scale bridging effect, and not from any intrinsic toughening mechanisms. However, this has not been experimentally verified.

As the fracture toughness testing was conducted on samples with fatigue pre-cracks, the measured values may differ from those measured from notched samples. While the plateau values (K_{Ic}) are likely to be more conservative due to the "atomically sharp" nature of the crack tip, the initiation values (K_{Ii}) may be higher, reflecting the highest K_{MAX} experienced during the fatigue test. For design considerations, K_{Ic} obtained from fatigue pre-cracked samples will represent the lower bound toughness value for the composite.

3.6.3. Microstructural Examination

Fracture surface comparisons between series P and series C samples under cyclic fatigue are displayed in Figures 3.13 through 3.15. *R*-curve fracture surface comparisons are displayed in Figures 3.16 through 3.18. Clearly evident in these fracture surfaces are the differences in failure mechanisms between the two series. Series C showed signs of brittle cleavage fracture in the matrix along with complete debonding at the particle interfaces. By contrast, series P fracture surfaces reveal a matrix dominated failure mode, with limited interfacial debonding. Of special note are the exposed fibrils lying on the fracture surfaces of series P samples (Figures 3.14d, 3.17f, 3.18d) indicating that crazing occurred during crack propagation, which is consistent with good interfacial strength leading to matrix failure. Shrinkage cracks were found in sample 100C (Figure 3.15a), a result of residual stresses within the sample.

Although minor differences exist between fatigue and *R*-curve fracture surfaces for each processing series, no evidence of fatigue striations or crack-arrest marking were

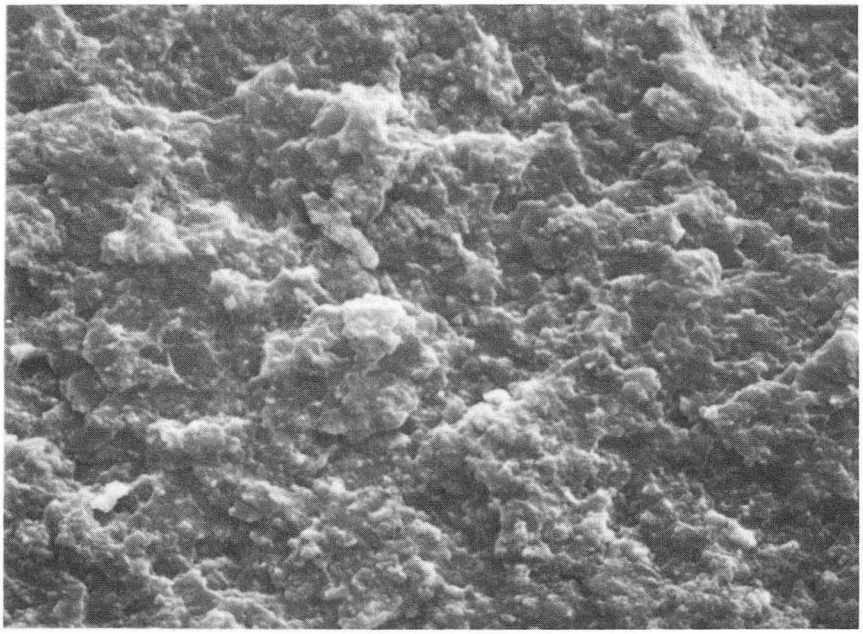

7 μm

Figure 3.13a Fatigue fracture surface, sample 1P.

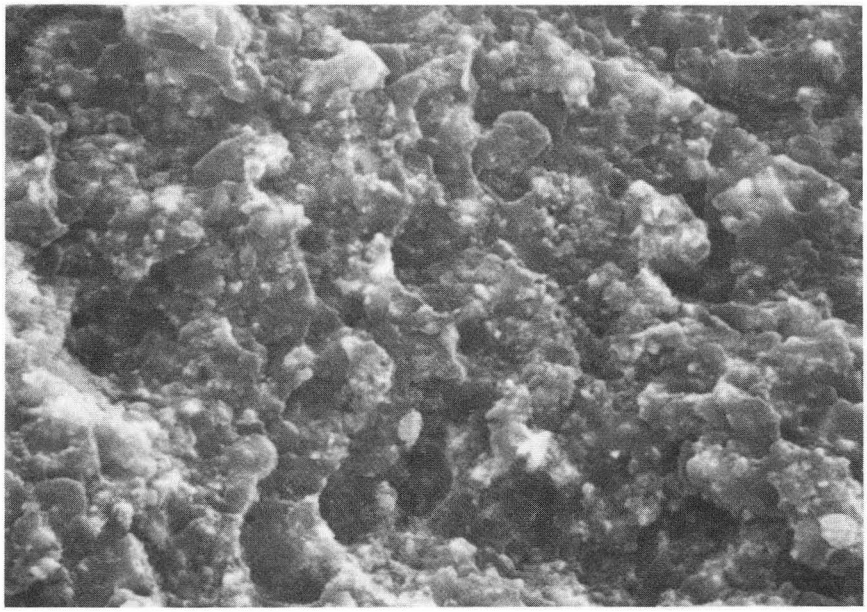

4 μm

XBB 905-3838

Figure 3.13b Fatigue fracture surface, sample 1P.

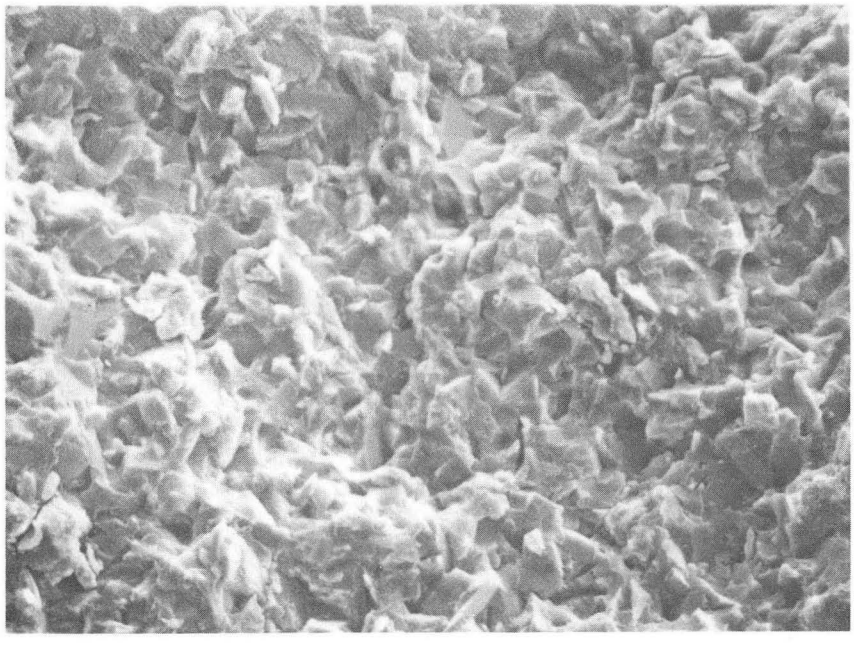

25 μm

Figure 3.14a Fatigue fracture surface, sample 16C.

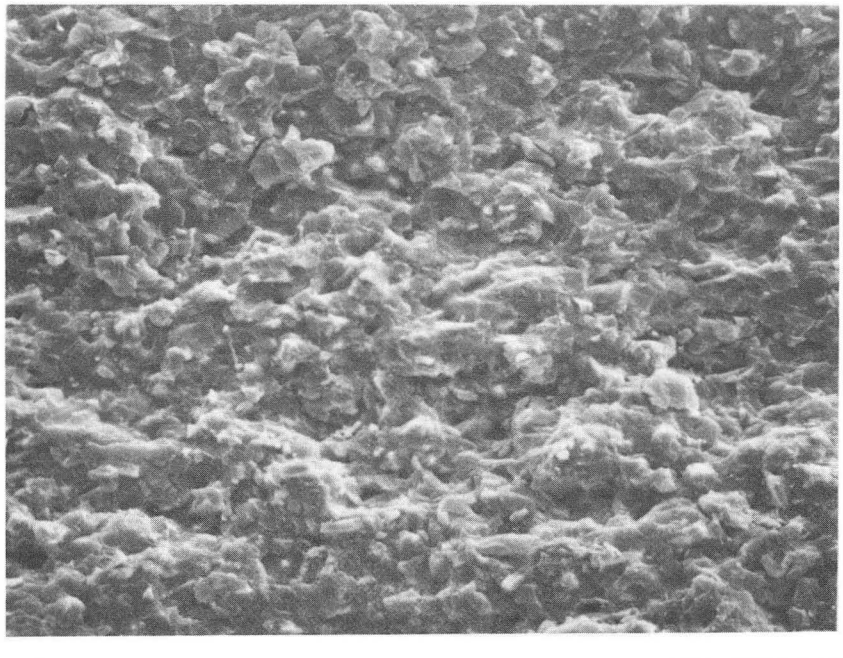

25 μm

XBB 905-3837

Figure 3.14b Fatigue fracture surface, sample 16P.

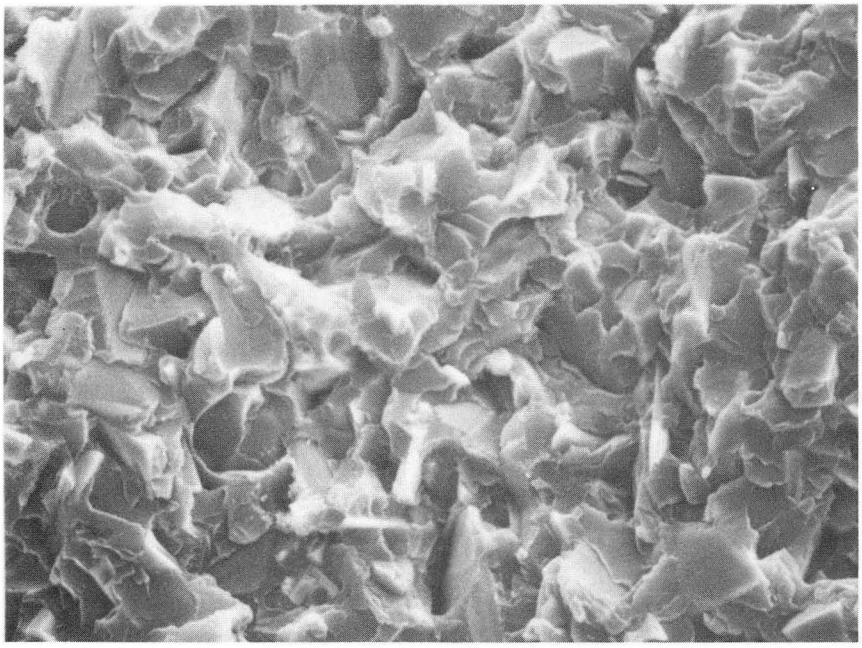

12.5 μm

Figure 3.14c Fatigue fracture surface, sample 16C.

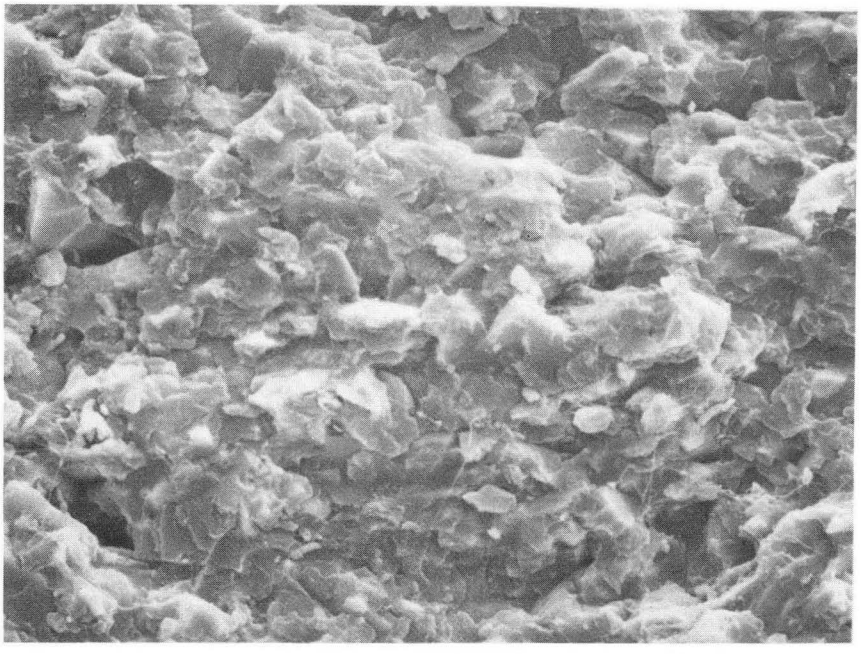

12.5 μm

XBB 905-3836

Figure 3.14d Fatigue fracture surface, sample 16P.

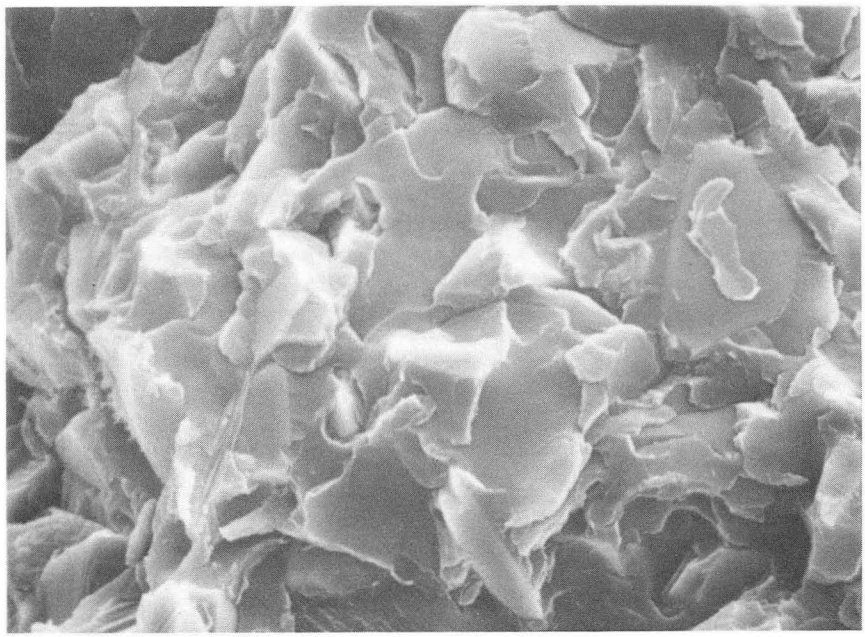

6 μm

Figure 3.14e Fatigue fracture surface, sample 16C.

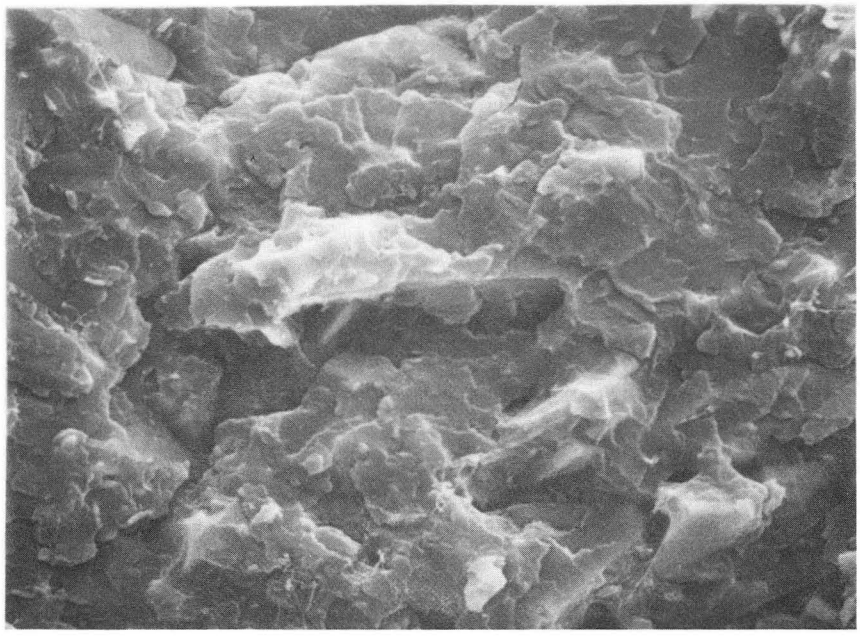

6 μm

XBB 905-3835

Figure 3.14f Fatigue fracture surface, sample 16P.

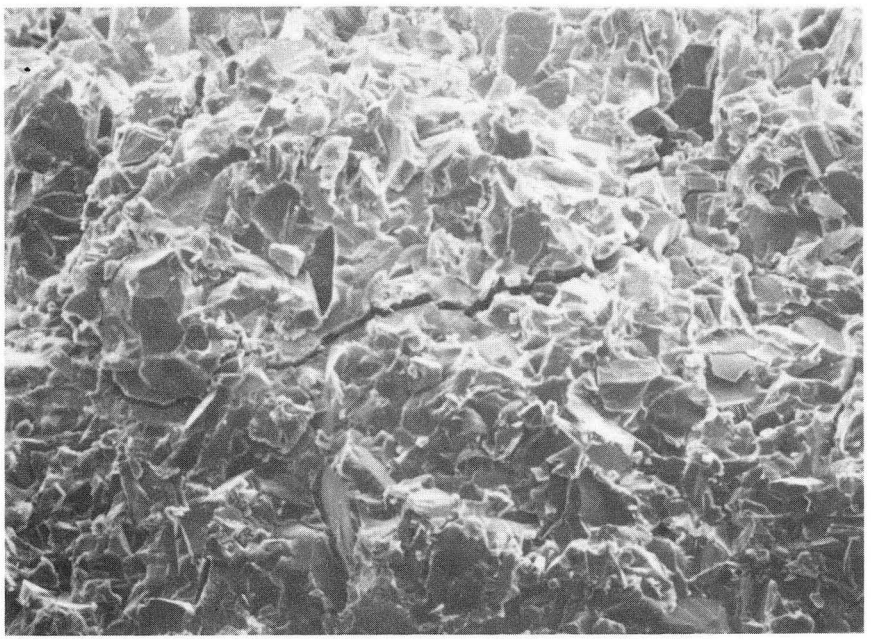

125 μm

Figure 3.15a Fatigue fracture surface, sample 100C.

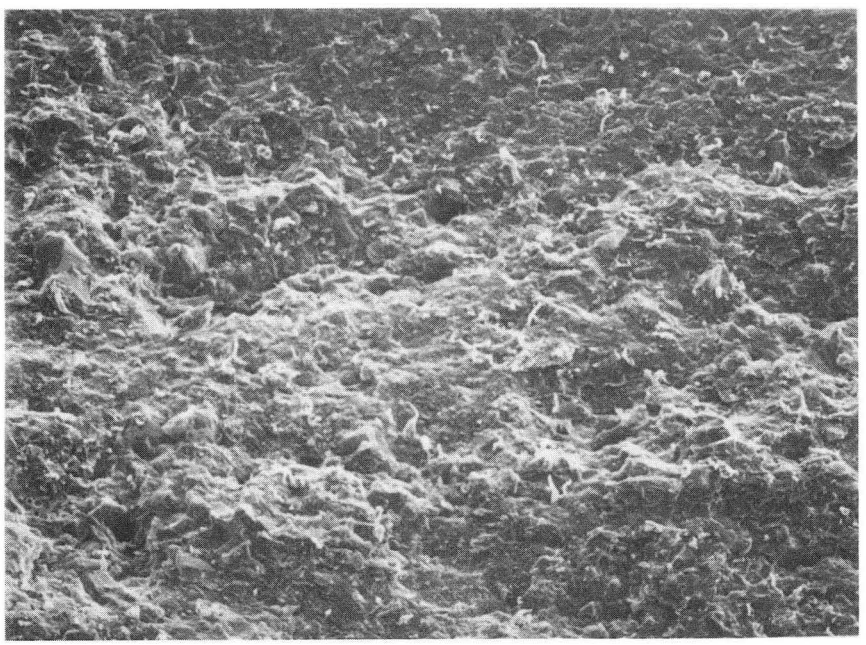

XBB 905-3834

125 μm

Figure 3.15b Fatigue fracture surface, sample 100P.

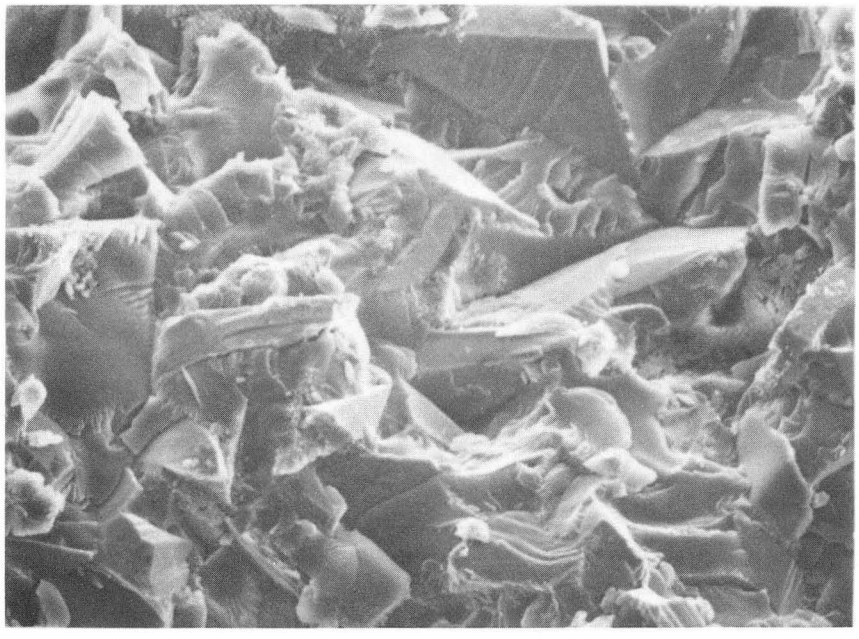

30 μm

Figure 3.15c Fatigue fracture surface, sample 100C.

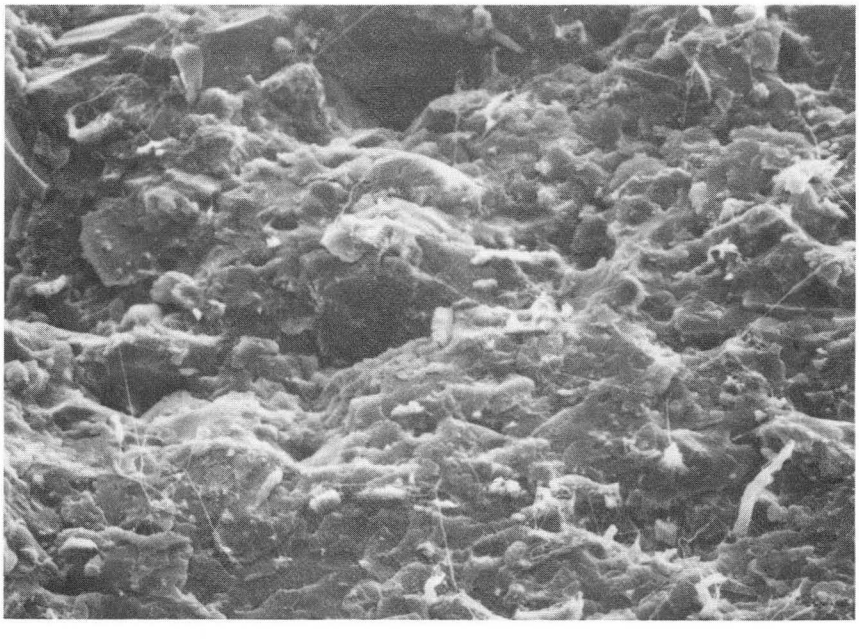

30 μm

XBB 905-3833

Figure 3.15d Fatigue fracture surface, sample 100P.

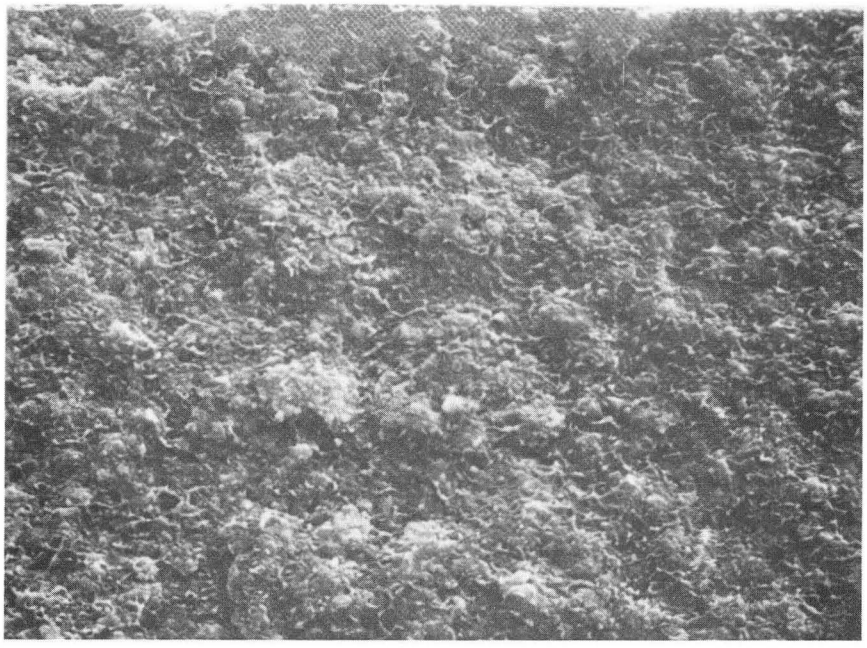

7 μm

Figure 3.16a *R*-curve fracture surface, sample 1P.

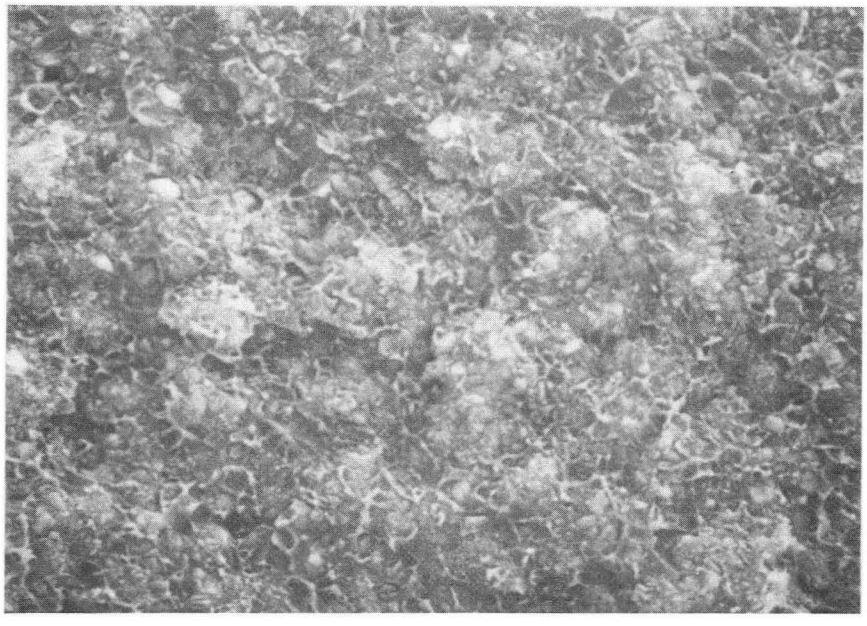

XBB 905-3832

4 μm

Figure 3.16b *R*-curve fracture surface, sample 1P.

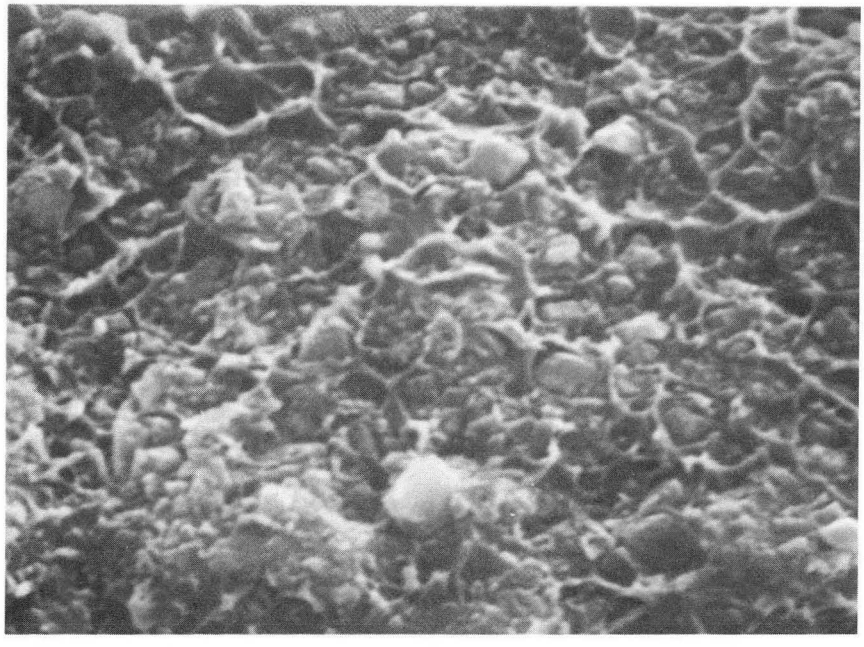

2 μm

XBB 905-3831

Figure 3.16c *R*-curve fracture surface, sample 1P.

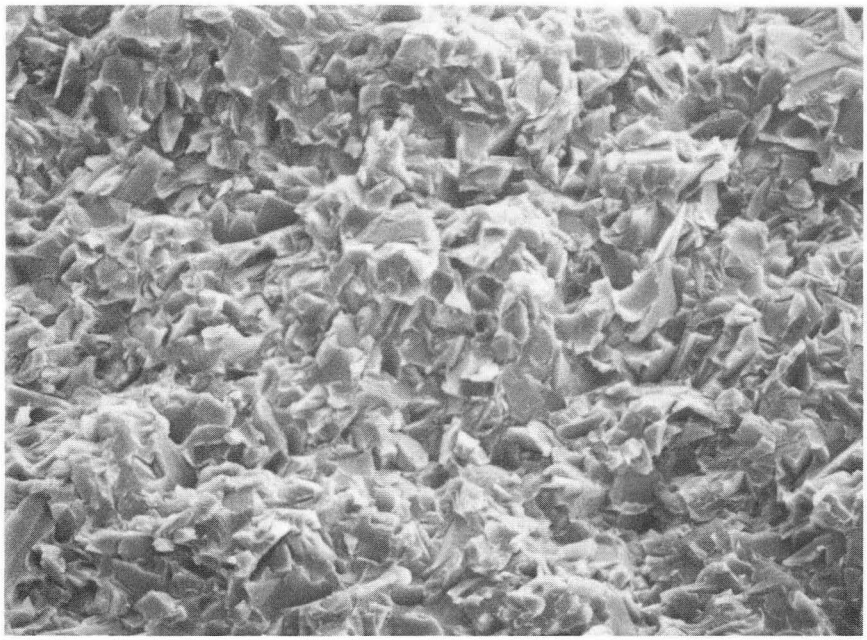

25 μm

Figure 3.17a Fracture surface, sample 16C.

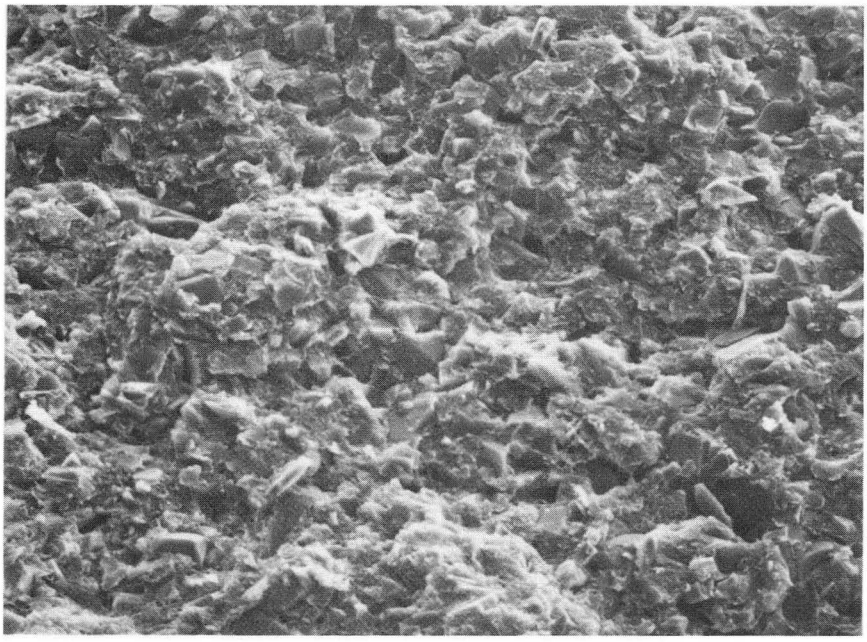

25 μm

XBB 905-3830

Figure 3.17b *R*-curve fracture surface, sample 16P.

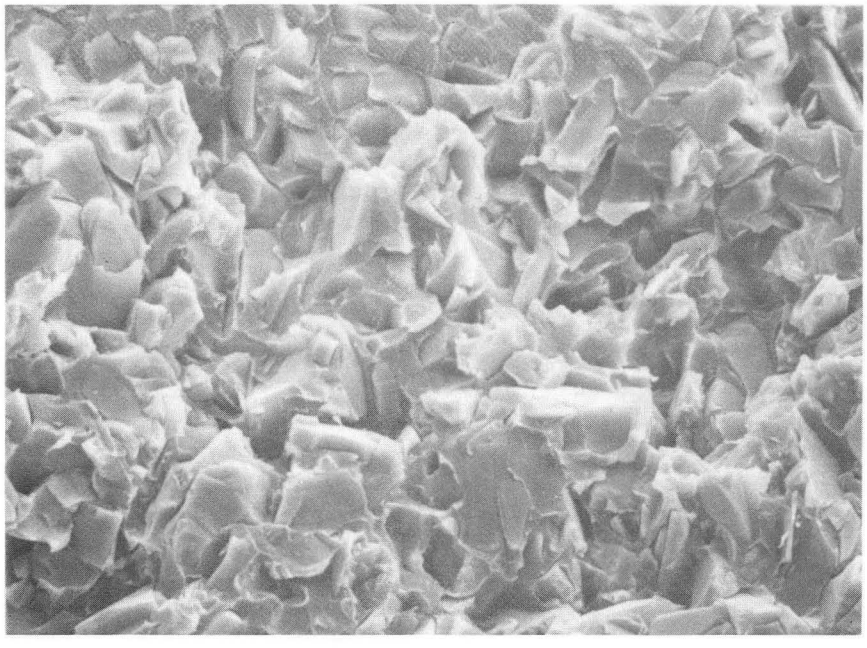

12.5 μm

Figure 3.17c Fracture surface, sample 16C.

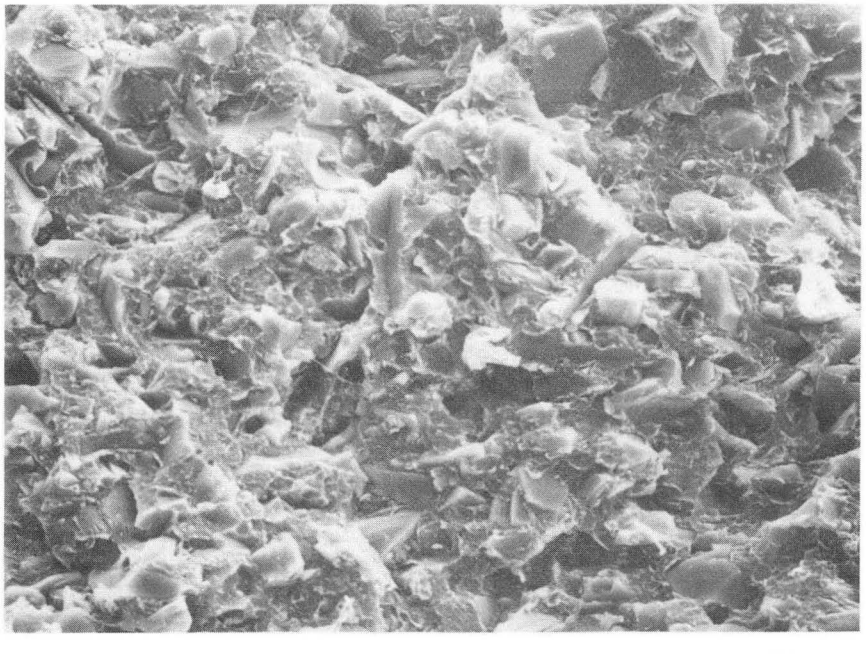

XBB 905-3829

12.5 μm

Figure 3.17d *R*-curve fracture surface, sample 16P.

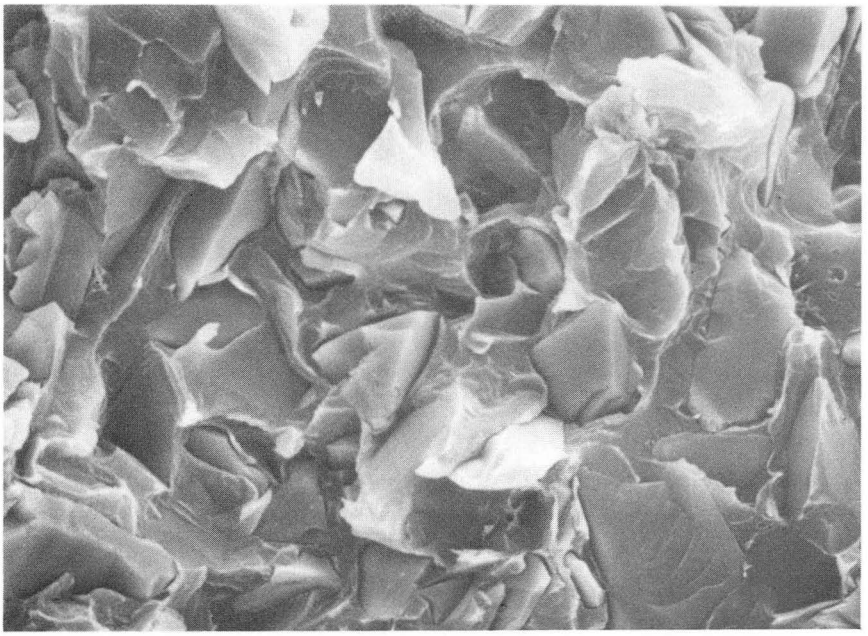

6 μm

Figure 3.17e Fracture surface, sample 16C.

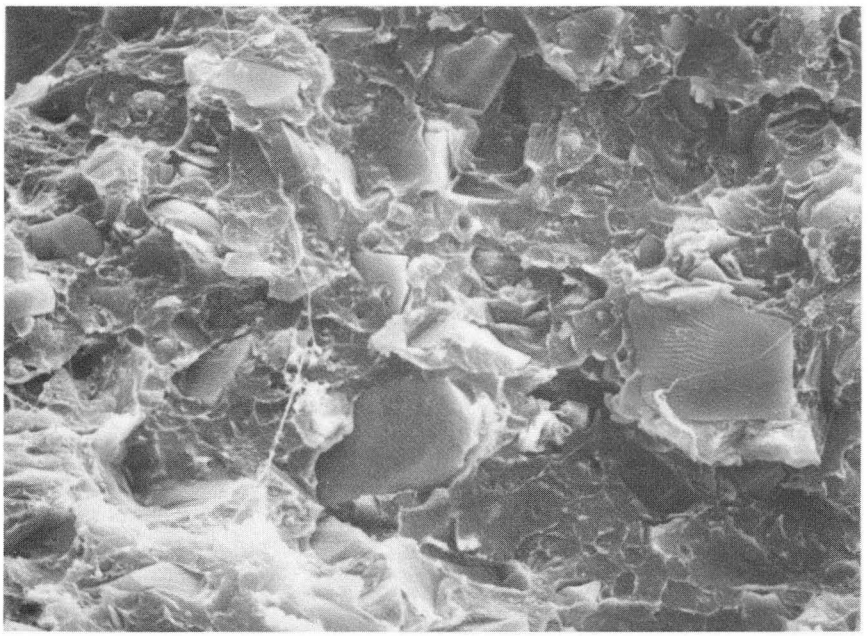

XBB 905-3828

6 μm

Figure 3.17f *R*-curve fracture surface, sample 16P.

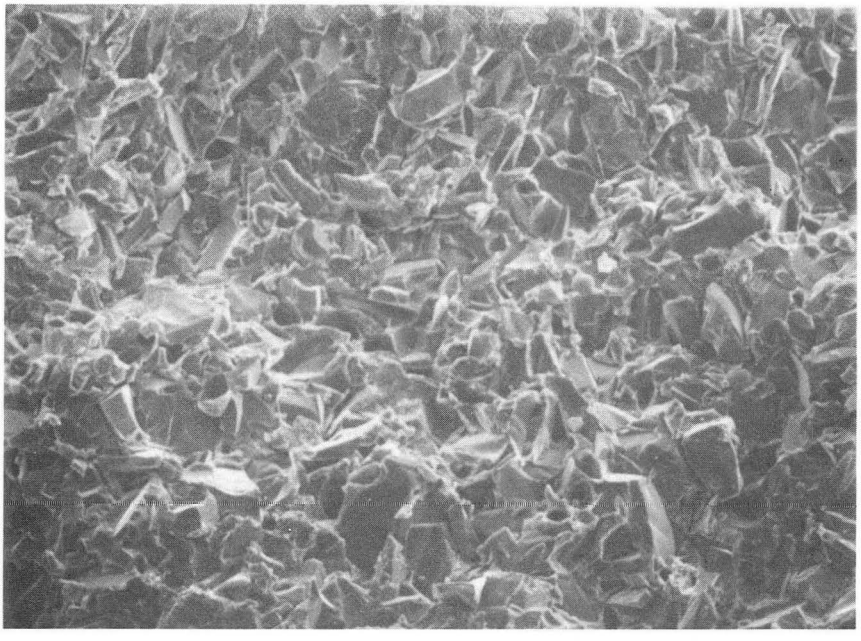

125 μm

Figure 3.18a *R*-curve fracture surface, sample 100C.

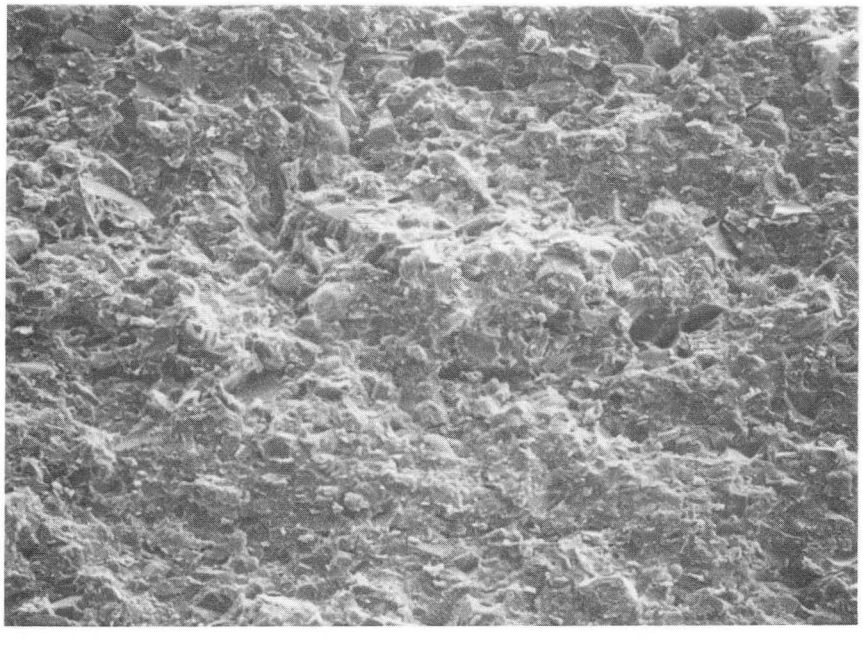

XBB 905-3827

125 μm

Figure 3.18b *R*-curve fracture surface, sample 100P.

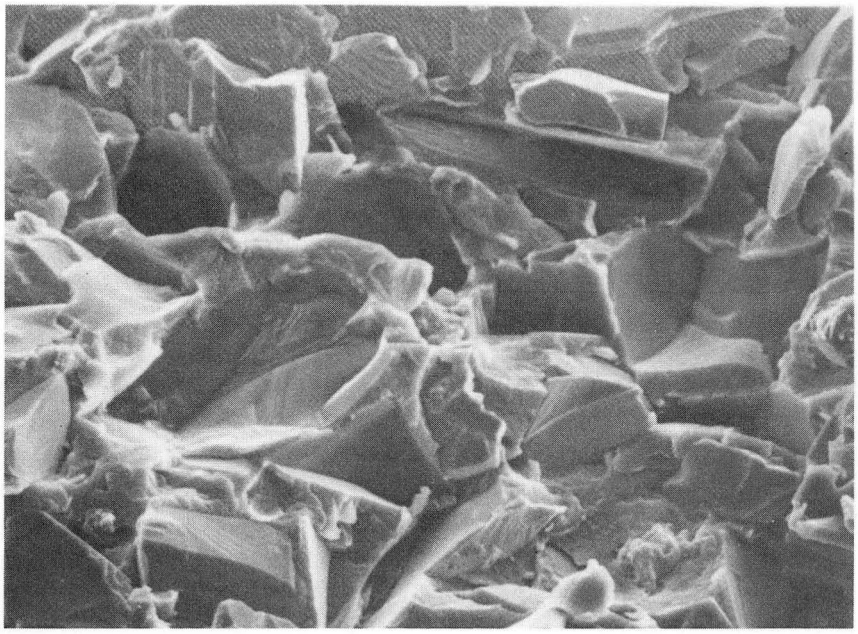

30 μm

Figure 3.18c *R*-curve fracture surface, sample 100C.

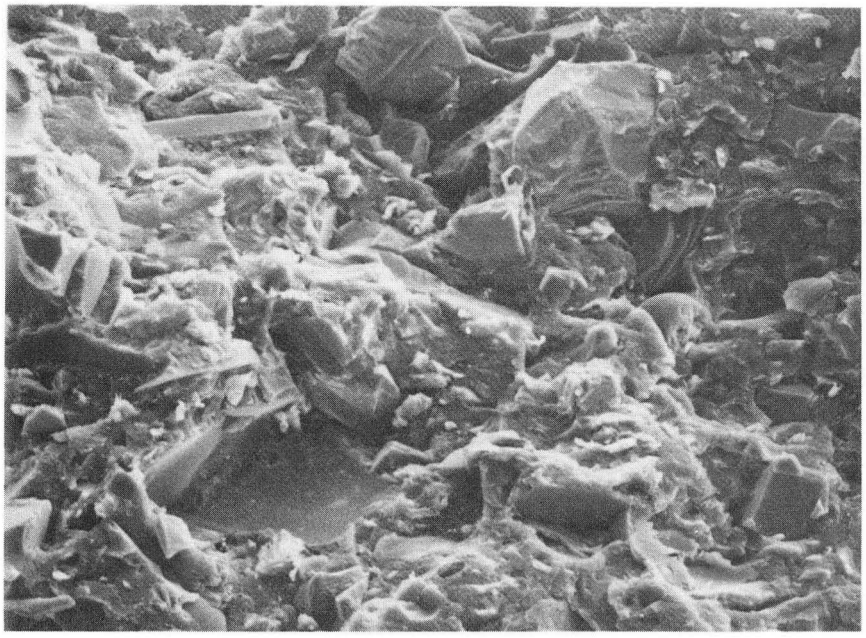

XBB 905-3826

30 μm

Figure 3.18d *R*-curve fracture surface, sample 100P.

observed that could differentiate the cyclic-fatigue growth regions from static growth regions. Evidence for both crack bridging by overlapping (A) and co-planar (B) ligaments can be seen in a typical crack profile (Figure 3.19). The crack profile clearly demonstrates the existence of these toughening mechanisms.

3.7. Discussion

Reinforcement appears to have enhanced the crack propagation resistance of samples containing 16 and 100 μm particles, while not improving the 1 μm sample as significantly when compared to unreinforced PMMA. SEM micrographs of the fracture surfaces of sample 1P indicate that the SiC reinforcement may, in fact, have acted as flaw initiation sites. This can be clearly seen in Figure 3.16, where failure is reminiscent of ductile rupture in metals. In many cases, SiC particles can be found within the cups formed by the rupture, analogous to inclusions in steel. Such fracture surfaces would be expected as there is a loss of load bearing section in the sample. It is therefore concluded that the 1 μm particle size is ineffective for enhancing the crack propagation resistance of the composite, and may indeed be detrimental.

With the exception of sample 1P, the fatigue-crack growth rates for both the encapsulation processed and conventionally cast samples fall into a relatively narrow range, indicating that the toughening mechanisms involved are not as potent in fatigue as under static loading conditions. In addition, the trend of increasing toughness with increasing particle size demonstrates that crack bridging and shielding are more effective when particle sizes increase, consistent with the results of Shang.[63] This is to be expected, as a larger bridging zone is produced by larger particles and a more tortuous crack path taken due to deflection.

Analysis of the fracture surfaces of the C series samples implies the existence of shrinkage stresses. The complete interfacial debonding observed suggests that the particle-matrix interface is under residual tension, which weakens the interface. These weakened

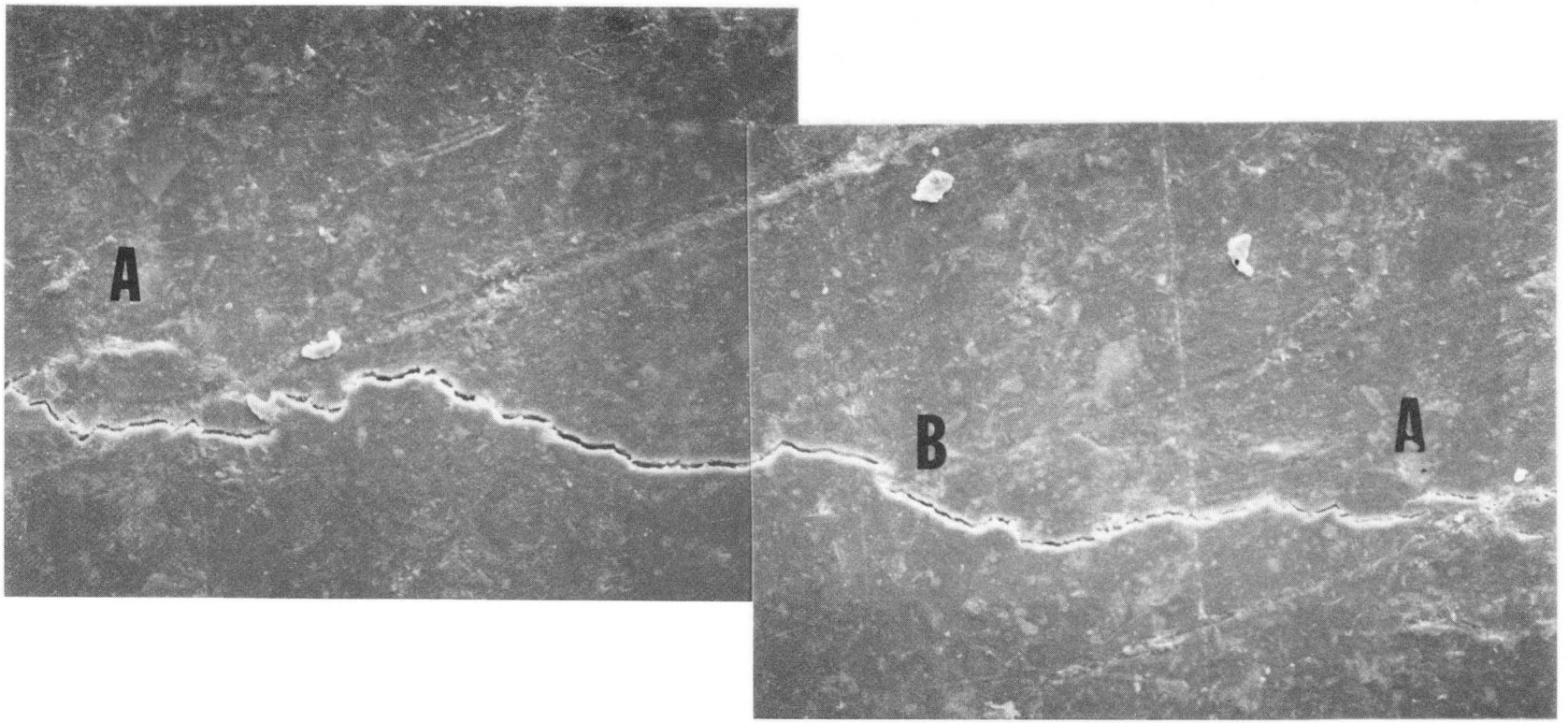

XBB 905-3825

50 mm

Figure 3.19 Typical crack profile showing crack bridging by overlapping ligaments (A) and co-planar ligaments (B).

interfaces debond at much lower applied stress levels. Although debonding increases crack shielding due to process zone wake dilation, the severe material degradation that occurs in the frontal process zone strongly limits the toughness enhancement and may produce an overall weakening of the material.

The stress state of the cast samples can be rationalized by considering the effect of shear mix processing on these samples. Shear mixing requires mechanical agitation to provide the dispersion and wetting of the second phase particles. In particular, wetting is highly dependent upon the surface area to be wet, as well as the viscosity of the wetting liquid. In addition, the stability of the suspension must be considered. A high viscosity solution will be more effective in suspending the second phase particles. Therefore, the process parameters must be balanced between these three variables. As the particle size changes, the surface area to be wet varies according to Figure 3.20, assuming idealized spherical particles. It is clear that viscosity must decrease with particle size. This is most easily accomplished by introducing the particles earlier in the polymerization process.

Mixing at an early stage of polymerization introduces a new processing variable: the degree of monomer to polymer conversion. There is a volume change (ΔV) of 28% associated with the polymerization of methyl methacrylate, as determined by the ratio of densities (ρ_{MMA}=0.936 g/cc, ρ_{PMMA}=1.2 g/cc). At an early stage of polymerization, the majority of the contraction has yet to occur. The result is the introduction of large shrinkage stresses that weaken the interface. In the system depicted in Figure 1.2, the matrix is constrained from shrinking by both the mold walls and the dispersed particles, with the bulk of the constraint imposed by the walls. These constraints produce tensile stresses within the matrix in all three dimensions. These tensile stresses weaken the particle-matrix interface, resulting in poor mechanical properties.

This phenomenon can be seen in the large shrinkage cracks observed in sample 1C. Going to higher degrees of polymer conversion resulted in mixtures that were too viscous to coat the particles effectively or cast in a mold. The 100C sample did not display this

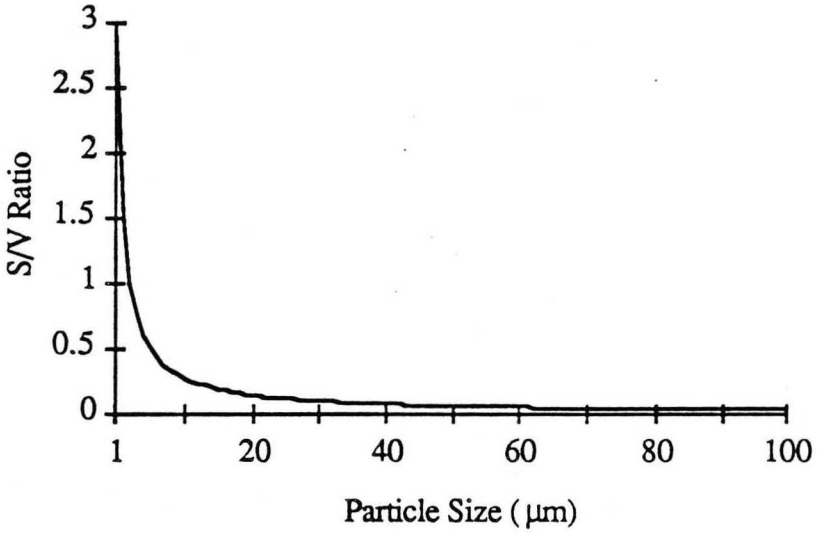

Figure 3.20 Surface to volume ratio as a function of particle size. The particles are assumed to be spherical.

behavior. For large second phase particles, a high viscosity is required to prevent settling. Thus a high degree of polymerization must be allowed to develop before introducing the particles. This results in a small ΔV following cast. It is therefore expected that the shrinkage stresses should decrease with increasing particle size.

One unexpected result is the superior fatigue resistance of sample 16C. This must be qualified, however, because the data did not provide an accurate characterization of the fatigue behavior of this sample. No characteristic fatigue threshold (ΔK_{TH}) was observed, inconsistent with the other samples. Rather, the growth rate continued to increase even as the applied ΔK decreased. This phenomenon may also be explained by considering shrinkage stresses. As the mold walls constitute a rigid constraint for the polymerizing system, tensile stresses will develop. However, regions far removed from the walls will experience little constraint, as the reinforcement particles are not rigidly fixed. Therefore, stress relief and even the formation of residual compressive stresses may occur within the center of the sample. The result is a radial stress gradient which affects the fatigue behavior of the sample. Initial crack growth occurs at the notch tip in the center of the sample. As the crack propagates, the residual tensile region will be reached. Even as the applied ΔK decreases, the effect of the weakened interface causes the crack to accelerate. This would lead to unexpected catastrophic failure, which occurred with sample 16C. No threshold can be reached, as the equipment cannot decrease ΔK quickly enough to arrest crack growth.

The encapsulation processed samples have much lower residual stress levels due to the method of processing. While some interfacial weakening may occur, it is minimized by the pressure applied during forming and subsequent cooling. This pressure provides the driving force for uniform shrinkage in the samples, offsetting thermal expansion mismatch. The particle-matrix interface therefore stays intact to much higher applied stress levels. SEM micrographs confirm that the failure mode is a mixture of matrix crazing and interfacial debonding. For the case of crack shielding, the decrease in the fraction of

debonded particles means that the toughness contribution from the process zone wake diminishes. However, this is partially compensated by the reduced material degradation occurring ahead of the crack tip, resulting in less crack advance. In addition, good interfacial adhesion activates other toughening mechanisms, such as crack pinning.[31] This would naturally lead to higher measured toughness values.

The effects of reinforcement particles on the toughness properties of a composite are generally complex, and interactions between toughening mechanisms can complicate the picture even more. Although it is difficult, if not impossible to distinguish contributions to toughening by these various mechanisms, the results can be clearly seen in the K_{Ic} values obtained from samples 100P and 100C. A significant toughening increase was observed for the encapsulation processed 100P sample over the conventionally cast 100C sample.

In many instances, interactions between mechanisms can produce synergism between the mechanisms and be highly beneficial.[64] These synergism effects are most likely to occur when process zone and bridging mechanisms interact.[65] However, detailed analysis of such coupling effects have yet to be made.

4. Summary

A process for the encapsulation of silicon carbide with polymethyl methacrylate was successfully developed using the precipitation encapsulation technique. The precipitation of PMMA onto the SiC substrate was controlled by adjusting the number of available nucleation sites followed by decreasing the concentration of monomer in solution. The encapsulated powders were subsequently formed by compaction with applied heat, into composites having uniform distributions of silicon carbide and containing relatively low residual stress levels as compared to the cast samples.

Mechanical testing of the composites has shown an increase in crack growth resistance with increasing particle size. In addition, the encapsulation processing route produced composites with significantly increased fracture toughness over conventionally cast composites, while the fatigue crack propagation behavior remained essentially unchanged. Decreases in residual stress levels within the sample resulted in improved interfacial adhesion, thereby promoting crack bridging and deflection, while somewhat reducing process zone wake shielding. In addition, crack pinning may have also made a significant contribution to toughening under conditions of limited debonding.

With regard to fatigue and fracture toughness test results, the multiplicity of toughening mechanisms that may be simultaneously active makes the isolation of any single mechanism extremely difficult, if not impossible. The magnitude of contribution from each mechanism to toughening is therefore not immediately obvious. However, general trends may be correlated with the observed fracture features to deduce mechanisms that are contributing to toughening.

References

1. J.G. Mohr, S.S. Oleesky, G.D. Shook & L.S. Meyer, *SPI Handbook of Technology and Engineering of Reinforced Plastics/Composites* (Van Nostrand Reinhold Co., New York, 1973).

2. H.S. Katz & J.V. Milewski, *Handbook and Fillers and Reinforcements for Plastics* (Van Nostrand Reinhold Co., New York, 1978).

3. J.M. Crosby, *Adv. Mater. Processes* **133**, 56-59 (1988).

4. J.D. Bolt & R.H. French, *Adv. Mater. Processes* **134**, 32-35 (1988).

5. J.A. Black, *Adv. Mater. Processes* **133**, 51-54 (1988).

6. S.S. Oleesky & J.G. Mohr, *SPI Handbook of Reinforced Plastics of the Society of the Plastics Industry* (Reinhold Publishing Corp., New York, 1964).

7. S. Turner, *Appl. Mat. Res.* **4**, 10-19 (1965).

8. W.C. Dillard & A. Lou, *Adv. Mater. Processes* **134**, 33-36 (1988).

9. L. Nicolais & L. Nicodemo, *Intern. J. Polymeric Mater.* **4**, 229-243 (1974).

10. Z.R. Lindeman, D. Witemberg-Perzyk & M.A. Perzyk, *J. Reinf. Plast. Compos.* **1**, 3-15 (1982).

11. V.A. Tochin, E.N. Shchupak, V.V. Tumanov, O.B. Kulachinskaya & M.I. Gai, *Mech. Compos. Mater.* **21**, (1985).

12. P.K. Mallick & L.J. Broutman, *Mat. Sci. Eng.* **18**, 63-73 (1975).

13. S. Sahu & L.J. Broutman, *Polymer Eng. Sci.* **12**, 91-100 (1972).

14. V.E. Zgaevsky, *Intern. J. Polymeric Mater.* **6**, 109-124 (1977).

15. C.W. Van Der Wal, H.W. Bree & F.R. Schwarzl, *J. Appl. Pol. Sci.* **9**, 2143-2166 (1965).

16. R.F. Landel & T.L. Smith, *American Rocket Society Jnl.* **31**, 599-608 (1961).

17. L.L. Anderson, *Polym. Eng. Sci.* **28**, 522-528 (1988).

18. Z.U. Haque & D.T. Turner, *J. Mat. Sci.* **22**, 3379-3384 (1987).

19. B. Turcsanyi, B. Pukanszky & F. Tudos, *J. Mat. Sci. Lett.* **7**, 160-162 (1988).

20. D.K. Das-Gupta & M.J. Adbullah, *J. Mat. Sci. Lett.* **7**, 167-170 (1988).

21. B. Jalajakumari, K.G. Warrier, K.G. Satyanarayana & C. Pavithran, *J. Reinf. Plast. Compos.* **7**, 402-412 (1988).

22. C.S. Saunders Jr, *Ceramic Industry* **133**, 35-37 (1989).

23. J.G. Zhang, M.J. Edirisinghe & J.R.G. Evans, in *Complex Microstructures '88,* 91-99 (The Institute of Ceramics, Durham University, Durham, 1988).

24. L.C. DeJonghe, M.N. Rahaman & M. Lin, *Ceramic Microstructures '86,* 447-454 (Plenum Publishing, 1986).

25. P. Eliades, *Engineering* **227**, 719-722 (1987).

26. J.C. Anderson & A. Davies, *Lubr. Eng.* **40**, 41-46 (1984).

27. Y.A. Dzenis, *Mech. Compos. Mater.* **22**, 12-19 (1986).

28. L.E. Nielsen, *J. Comp. Mater.* **1**, 100-119 (1967).

29. R.H. Dauskardt & R.O. Ritchie, *Closed Loop* **17**, 7-17 (1989).

30. L.E. Hornberger & K.L. DeVries, *Poly. Eng. Sci.* **27**, 1473-1478 (1987).

31. A.G. Evans, *Ceramic Containing Systems - Mechanical Aspects of Interfaces and Surfaces* (Noyes Publications, Park Ridge, NJ., 1986).

32. J.K. Shang & R.O. Ritchie, *Met. Trans. A* **20**, 897-908 (1989).

33. S.H. Emerman, *Polym. Eng. Sci.* **27**, 1105-1111 (1987).

34. H.H. Hausner & M.K. Mal, *Handbook of Powder Metallurgy* (Chemical Publishing Co. Inc., New York, 1982).

35. G.W. Poehlein, in *Applied Polymer Science,* 1-1341 (American Chemical Society, Washington, D.C., 1985).

36. J. Ugelstad, F.K. Hansen & S. Lange, *Makromol. Chem.* **175**, 507-521 (1974).

37. M.K. Lindeman, in *Vinyl Polymerization* (Dekker, New York, 1967).

38. K. Furusawa, Y. Kimura & T. Tagawa, in *Polymer Adsorption and Dispersion Stability,* 1-477 (American Chemical Society, Washington, D.C., 1984).

39. J.N. Coker, *Polymer Coated Pigment Particles and a Process for Their Preparation* (1975), U.S. Patent #3,897,586.

40. M.N. Rahaman, Y.P. Boiteux & L.C. DeJonghe, *Ceram. Bull.* **65**, 1171-1176 (1986).

41. Y.P. Boiteux, M.S. Thesis, University of California, Berkeley (1986), *Surface Characterization and Manipulation of Si_3N_4 and SiC Powders* .

42. F.F. Lange, *Phil. Mag.* **8**, 983-992 (1970).

43. A.G. Evans, *Phil. Mag.* **8**, 1327-1344 (1972).

44. G.M. Newaz, *J. Mater. Sci. Lett.* **5**, 71-72 (1986).

45. F.F. Lange & K.C. Radford, *J. Mater. Sci.* **6**, 1197-1203 (1971).

46. R. Maxwell, R.J. Young & A.J. Kinloch, *J. Mater. Sci. Lett.* **3**, 9-12 (1984).

47. A.J. Kinloch, D.L. Maxwell & R.J. Young, *J. Mater. Sci.* **20**, 4169-4184 (1985).

48. F.F. Lange, *J. Amer. Ceram. Soc.* **54**, 614-619 (1971).

49. D.J. Green, P.S. Nicholson & D.J. Embury, *J. Mater. Sci.* **14**, 1413-1420 (1979).

50. L.J. Broutman & S. Sahu, *Mater. Sci. Eng.* **8**, (1971).

51. H. Ruf & A.G. Evans, *J. Am. Ceram. Soc.* **66**, 328 (1983).

52. A.G. Evans, *Advances in Ceramics* **12**, 193 (1983).

53. R.W. Hertzberg, *Deformation and Fracture Mechanics of Engineering Materials* 1-682 (John Wiley and Sons, New York, 1989).

54. A.G. Evans & K.T. Faber, *J. Amer. Ceram. Soc.* **67**, 255-260 (1984).

55. B. Budiansky, J.W. Hutchinson & A.G. Evans, *J. Mech. Phys. Solids* **34**, 167-189 (1986).

56. J.K. Shang & R.O. Ritchie, *Crack-Tip Shielding in Metal-Matrix Composites: Modelling of Crack Bridging by Uncracked Ligaments* 1-81-87 (Materials Research Society, 1988).

57. P.S. Theocaris, G.C. Papanicolaou & E.P. Sideridis, *J. Reinf. Plast. Compos.* **1**, 92-106 (1982).

58. E. Alfthan, A.d. Ruvo & M. Rigdahl, *Intern. J. Polymeric Mater.* **7**, 163-166 (1979).

59. G.C. Papanicolaou, S.A. Paipetis & P.S. Theocaris, *J. Appl. Pol. Sci.* **21**, 689-701 (1977).

60. K. Kendall, *J. Mat. Sci.* **22**, 4514-4517 (1987).

61. P.K. Liaw, H.R. Hartmann & W.A. Logsdon, *J. Testing Eval.* **11**, 202-207 (1983).

62. P.C. Paris & F. Ergdogan, *ASME J. Basic Eng.* **85**, 528-534 (1963).

63. J.K. Shang, W. Yu & R.O. Ritchie, *Mat. Sci. Eng. A* **102**, 181-192 (1988).

64. J.C. Amazigo & B. Budiansky, *J. Mech. Phys. Solids* **36**, 581-595 (1988).

65. A.G. Evans, *J. Am. Ceram. Soc.* **73**, 187-206 (1990).

LAWRENCE BERKELEY LABORATORY
UNIVERSITY OF CALIFORNIA
INFORMATION RESOURCES DEPARTMENT
BERKELEY, CALIFORNIA 94720